DEVELOPING OPTICAL PTYCHOGRAPHY FOR BIOPHYSICAL APPLICATIONS

Università degli Studi di Genova

PhD in Physics and Nanoscience

Tutor:

Prof. Alberto Diaspro

Supervisors:

Dr. Nicholas Anthony, Dr. Salvatore Surdo

PhD candidate

Alberta Trianni

XXXIV Doctorate Cycle

Abstract

Phase contrast (PC) microscopy offers notable opportunities for optical label-free studies in cellular biology. Indeed, the phase of light travelling through a sample provides a contrast mechanism, which codes its thickness (morphology) or refractive index (biochemistry). As such, PC methods allow imaging transparent biological samples without causing photobleaching and phototoxicity as in fluorescence microscopy. However, quantitative phase contrast methods, e.g., differential interference contrast microscopy, are based on interferometry. This architecture is sensitive to misalignments between the probe and reference beams, external disturbances, and its integration into other microscopes can be complicated and costly.

A method capable of solving the above problems is ptychography, namely a computational microscopy technique that computes the phase and amplitude of light waves probing a target sample by analyzing multiple diffraction patterns. Compared to other PC methods, ptychography has unique features: 1) the experimental setup can be as simple as a light source and camera; as such, the technique can be integrated into a large variety of microscopes with minimal additional optics; 2) Ptychography applies to thin and thick samples, as well; 3) returning both amplitude and phase images, ptychography is inherently a multimodal system.

This thesis aims at exploiting optical ptychography as a label-free tool for biological studies. To this end, we designed and characterized a compact ptychography microscope, which can be easily integrated into other microscopes leading to a multimodal imaging system. We found that our ptychographic system has excellent phase contrast sensitivity (5.34×10^6 rad/m·RIU) and low detection limit (8.8×10^{-7} m·RIU). Following this result, we used ptychography to study genetic diseases. As a case of study, we selected the Hutchinson-Gilford progeria syndrome based on the rationale that healthy, and progeria cells have different chromatin compactions and thus different refractive indices. As our results indicate, ptychography measured notable differences between the phase of healthy and unhealthy cells, which were confirmed by multimodal measurements comprising confocal and light-polarized microscopy.

Although we are aware that there is still room for improvements– the spatial resolution of our system is a point requiring future works– this thesis undoubtedly is a significant step forward in the realization of a totally label-free multimodal microscope for advanced biological studies.

Contents

Preface

Motivation and aim of the work

From its invention in the 17th century, the optical microscope has made possible what was not, namely seeing the "invisible", gradually pushing our observations down to the nanoscale. Over the years, optical microscopy has evolved to resolve the smallest details of an object by exploring different contrast mechanisms of biological and material samples. The main difference between the existing methods lies in the origin of the collected light. In general, one can distinguish two broad groups: fluorescence methods and label-free methods.

Fluorescence methods collect photons emitted by fluorescent probes, which are chemically bound to a target sample. In this way, fluorescence microscopy not only provides specificity but also the possibility to investigate different processes at the same time using multicolor staining, as well as the ability to overcome the diffraction limit reaching super-resolution, though, this usually comes at the expense of cost and complexity of the microscope architecture. Moreover, fluorescence microscopy is limited by several drawbacks, such as excessive sample manipulation resulting in artifacts and phototoxicity. On the contrary, label-free methods exploit changes in light properties such as polarization, amplitude, or phase, which are naturally caused by the interaction of light with the sample. Among the possible choices, looking at the phase of light waves passing through the sample is a powerful tool to provide contrast. Phase contrast imaging techniques are often cheaper and allow studying the sample in its native state by using only the signal coming from the differences in thickness or refractive index that influence the phase shift and thus the contrast. Although useful, these methods also suffer from some limitations, mainly the poor spatial resolution and the lack of quantitative measurements. This latter represents an important factor in the analysis of the phase shift since it can give valuable insight into the investigation of biological processes. A possible technique that can provide quantitative phase measurements is ptychography, a computational microscopy

method that computes amplitude and phase of light waves interacting with a sample by processing multiple diffraction patterns. The technique of ptychography has gained more and more interest over the years, with applications ranging from electron microscopy to X-rays and optical wavelengths. This computational approach is able to quantitatively recover optical parameters of a sample (such as refractive index) starting from the measurement of its amplitude and phase. As such, ptychography can be used for imaging live biological cells and studying their behavior, e.g., growth, reproduction, and motility.

Here we are expanding the portfolio of biological applications of ptychography. Precisely, the aim of this thesis is to explore, both theoretically and experimentally, the potentialities of ptychography as an optical label-free method for performing quantitative biological studies with minimum hardware implementations onto any commercial microscope. The long-term goal was to use ptychography to quantify the refractive index of target cells and exploit this information to solve fundamental biological problems. Among others, we focused our attention on genetic disorders (i.e., the Hutchinson-Gilford progeria syndrome) and investigated the possibility of discriminating between healthy and unhealthy cells on the basis of their different level of chromatin compaction and, thus, refractive index.

Summary of the work

The thesis is organized in 4 Chapters. Chapter 1 introduces the readers to basic concepts about optical ptychography. Considering the wide audience of this thesis, which spans from physicists to engineers and biologists, we decide to bring the readers gradually to the key topic of the thesis. To this end, Chapter 1 has three main sections: 1) light-matter interactions, 2) optical microscopy, and 3) ptychography. The first section deals with the properties of visible light, including how they change when light interacts with matter and how the material's optical properties (i.e., the refractive index) influence such interactions. The optical microscopy section deals with the fundamental concepts of spatial resolution and contrast. It is used to introduce and underline the importance of label-free approaches for biological studies and why they represent a valid alternative to common fluorescence techniques. Finally, the ptychography section presents a bit of history of the technique and how it is able to retrieve the amplitude and phase of light

interacting with a target sample. This concept is further explored in Chapter 2, where we show the ptychographic microscope developed for this work and explain in detail the hardware and software needed to collect data and reconstruct both amplitude and phase images. The chapter also reports on the experimental characterization of the microscope in terms of spatial resolution and image contrast. Ptychography is able to quantify the phase shift of light, so from the data collected, it is possible to extract valuable information such as the thickness of the sample and its refractive index distribution. Chapter 3 demonstrates that this quantification can be used for measuring the refractive index and/or thickness of a sample. With a verified hypothesis, in chapter 4, we applied the technique to the investigation of a biological problem, namely, the Hutchinson-Gilford progeria syndrome. To be precise, we experimentally studied the possibility of coupling ptychography with other microscopy techniques leading to a comprehensive multimodal imaging system. The work ends with a critical analysis of the advantages and disadvantages of the technique and possible future works aiming at improving its performance.

1 Introduction to Ptychography

1.1 Light-matter interactions

Light is a physical phenomenon that allows seeing the objects surrounding us. Light-matter interaction produces different optical phenomena (e.g., reflection, refraction, and absorption), which we experience daily since they allow us to be sensitive to colors or focus light. The main characteristics or properties of light are essential to study what physically happens when light interacts with particles (e.g., atoms, molecules) that constitute matter. This interaction modifies the properties of light according to the materials' optical properties, so with a priori knowledge of the native properties of a light source, we can extract a large set of information about the material under observation. This is the purpose of optical microscopy investigations, where the light source can be as simple as a lamp or a laser beam of selectable intensity and specific wavelength, and the material (object in this case) can be any type of inorganic or organic sample. In this chapter, we will introduce the theory describing the interactions of light with matter, which are relevant for optical microscopy and, in particular, for ptychography.

1.1.1 Basics

In physics, light can be a wave as well as a particle, as described by the wave-particle duality, a concept introduced at the beginning of the XX century following the works of several scientists, including Einstein, Planck, de Broglie, Bohr, Schrödinger[1]. Splitting the dualism, the particle behavior of light is represented by photons. Photons have no mass, and each one carries a specific amount of energy. In comparison, wave behavior is represented by electromagnetic
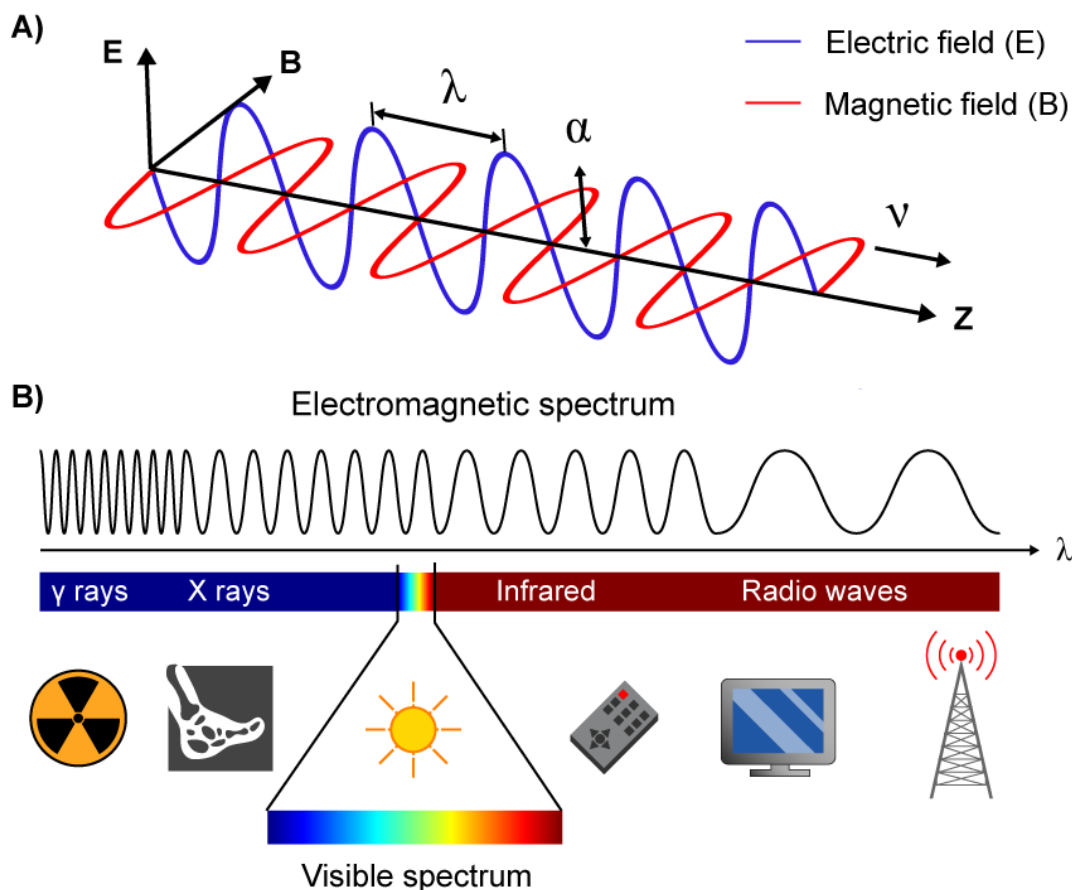
Figure 1.1. A) Propagation of an electromagnetic wave along the z-axis with velocity v, amplitude α, and wavelength λ. The electric field (E) is aligned to the y-axis, while the magnetic field (B) is along the x-axis. B) Diagram of the electromagnetic spectrum comprising electromagnetic radiations with increasing wavelengths and their possible applications, such as gamma rays and X-rays for medical diagnostics, visible and infrared light radiations for remote control, and radio waves for telecom applications.

radiations. Electromagnetic radiations are synchronized oscillations of electric and magnetic fields, one orthogonal to the other.

The fundamental properties that describe an electromagnetic wave are its wavelength and amplitude. As shown in Figure 1.1, the **wavelength** λ is the distance between two consecutive crests of the wave, and the **amplitude** is a measure of the change of a periodic variable in a single period. For a given material, the results of light-matter interactions can differ according to the choice of a specific light source or its wavelength. Therefore, this parameter can be selected
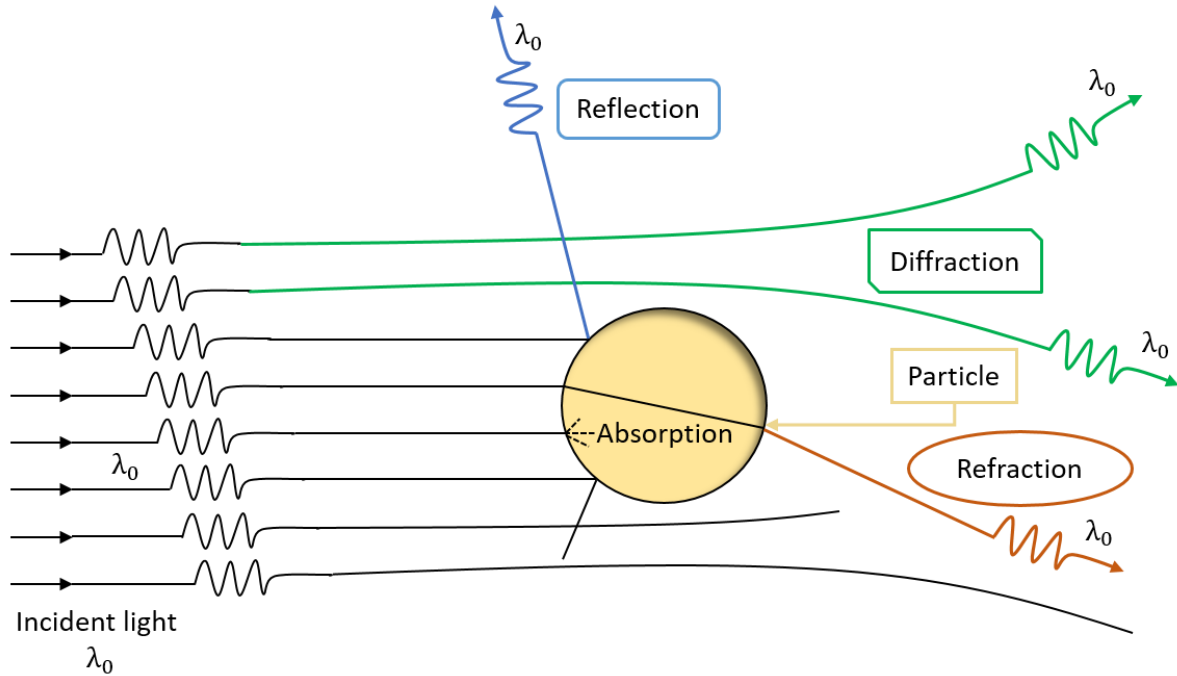
Figure 1.2. Schematic description of the possible interactions of a particle with a monochromatic electromagnetic wave; reflection (blue line), diffraction (green line), absorption (dashed black line), and refraction (red line).

to implement specific functionalities, as shown in Figure 1.1B. For instance, X-rays can be used for radiography, whereas infrared light can be used for telecom and visible light (λ from 380 nm to 750 nm) for optical microscopy. Once the wavelength λ is chosen, the results of light-matter interaction will depend on the material's optical and geometrical properties. In particular, for the simple case of a plane wave propagating along the z-direction in vacuum, the amplitude is:

$$A = \alpha cos(\varphi) = \alpha cos(kz - \omega t) \tag{1.1}$$

where, φ is the phase which is expressed in terms of the angular frequency ω, wave number $k = 2\pi/\lambda$, and time t. The interaction of light with a material might change these properties according to the material's characteristics. Possible outcomes of this interaction are shown in Figure 1.2 and include but are not limited to, changes in the direction of the wave (i.e., scattering and diffraction), reduction in the intensity (i.e., absorption), and variation of phase (i.e., phase shift) these latter due to wave propagation through the material. In general, the term scattering denotes a wide class of phenomena in which propagating light waves change their native direction after

light-matter interactions. From an energetic point of view, the scattering implies a change in energy and/or momentum of light. Depending on the geometries, size, and optical properties of the material, scattering can occur in either a random manner or a regular and predictable way. Below are a few basic descriptions of each of the possible light-matter interactions.

Reflection

Reflection is the change in the direction of the electromagnetic wave at the interface between two different media, causing a return into the medium where the wave originated. In this case, the angle of incidence is equal to the reflection one ($\theta_i = \theta_r$).

Refraction

Refraction denotes a change in the direction of propagation of a wave traveling through a medium whose optical property varies either gradually or abruptly. This latter case can be imagined as the passage of waves through the interface between two media. Refraction is a typical example of scattering affecting only the momentum of light. In particular, the change in velocity due to the discontinuity of refractive index leads to a change in the propagation direction according to Snell's equation:

$$n_i sin\theta_i = n_t sin\theta_t \tag{1.2}$$

where θi and θt are the angles of the incident and refracted light while ni and nt are the refractive indices of the two media. Simply put, Snell's law states that the greater the refractive index of a material, the larger is the light beam deflection or angle of refraction. Please note that here we are anticipating the concept of refractive index that will be detailed in the next section.

Diffraction

Diffraction denotes the bending of a wave around the edges of an aperture or an obstacle. The phenomenon of diffraction can be explained through the Huygens-Fresnel principle, which states that every point of a wavefront is a source of spherical wavelets spreading at the same speed of the original wave[2]. The sum of these wavelets or their envelope determines the wavefront formed behind the obstacle. In particular, the mutual interference between the wavelets leads to light intensity or diffraction patterns with bright and dark areas. The former result from wavelets interfering constructively, the latter from destructive interferences. The

occurrence of diffraction depends on the size (*d*) of the obstacle or aperture relative to the wavelength of light (λ). For wavelength much smaller than the obstacle size $\lambda<<d$, diffraction is almost imperceptible.

<u>Absorption</u>

The absorption is the ability of a material to reduce the intensity of electromagnetic radiation as it propagates through it. Absorption is related to *transmission* and *reflection* since the portion of the light that has not been absorbed is simply transmitted and/or reflected. The occurrence of absorption depends on the energy levels of the electrons of the material's atoms. Electrons have discrete energy levels or states, and providing them with the correct amount of energy, they can jump from one to another. In particular, when the electrons are in the lower energy level, it is said that they are in a *ground state*, while when they go into a higher energy level, they are in an *excited state*. The difference between these two levels is the energy gap. Absorption occurs when the photons' energy of incident light matches this gap.

1.1.2 Material properties

In the previous section, we have seen what happens when light passes through a material or encounters an obstacle. The question remains what is the material property that leads to the occurrence or set the extent of the phenomena we described. As anticipated above, the answer is the refractive index of the material. This property impacts both the speed and the amplitude of light waves passing through a material. The refractive index is a dimensionless complex number composed of a real part n_r and an imaginary part n_i:

$$n = n_r + i\, n_i \tag{1.3}$$

Considering again the simple case of a plane wave, equation 1.1 can be modified to account for the complex nature of the index of refraction as follow:

$$A = \alpha e^{-n_i z} cos(k n_r z - \omega t) \tag{1.4}$$

From equation 1.4, it is clear that the imaginary part n_i alters the amplitude of a light wave and the real part n_r its speed. Therefore, the imaginary part n_i is related to the loss of energy of the electromagnetic radiation and, thus, to light absorption.

Regarding the real part of the refractive index n_r, it can be defined as the ratio of the speed of light in vacuum $c = 3 \times 10^8$ m/s to the speed of light in the material v:

$$n_r = \frac{c}{v} \tag{1.5}$$

From equation 1.5, we can see that n_r modifies the wave number, meaning that waves that travel the same distance (L) in vacuum and in a medium accumulate different phases. We can refer to this difference as phase delay or *phase-shift*. As shown in Figure 1.3, for two media with different n values, the phase shift is equivalent to:

$$\Delta\varphi = \frac{2\pi}{\lambda} L(n_2 - n_1) \tag{1.6}$$

As detailed next, $\Delta\varphi$ is something that can't be easily revealed, meaning that it remains "invisible" to our eyes or traditional photodetectors. Indeed, the phase-shift is usually lost in microscopy techniques based on intensity measurements where the measured parameter is the square modulus of the electromagnetic field. Exceptions are few specific techniques dealing with the well-known problem of phase recovery, such as phase-contrast techniques and Ptychography, the latter being the main topic of this thesis.
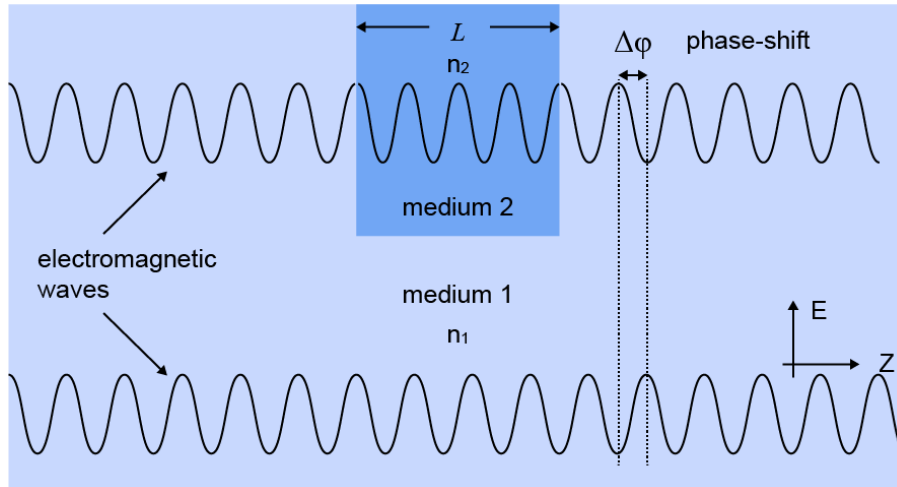

Figure 1.3. Schematic representation of the accumulation of a phase shift between two waves traveling through two materials with refractive index n_1 and n_2, respectively.

1.2 Optical Microscopy

The invention of the optical microscope can be dated back to the 17th century when Antoni Philips van Leeuwenhoek used a magnifying glass to project the image of an object onto the retina of his eyes[3]. After perfecting the system, this allowed van Leeuwenhoek to see for the first time objects inaccessible to the naked eye, such as microbes or bacteria. Starting from this very simple configuration, several scientists contributed to the development of new and better performing instruments. Famous examples include the works of Janseen, Hook and Galilei, which led to the invention of the first compound microscope. Even though modern systems provide higher levels of automation and a wider range of functionalities, the fundamental architecture of conventional optical microscopes is still the same. However, various implementations have been proposed over the years to improve the performance of an optical microscope in terms of spatial resolution and image contrast.

1.2.1 Resolution limit

The concept of resolution is the capability of an optical imaging system to distinguish fine details of a sample. It is defined as the shortest distance between two points that can be resolved as separate entities when imaged by the system. The spatial resolution of a conventional optical microscope is limited by diffraction; an optical system with resolution performance at its theoretical limit is said to be diffraction-limited.

The key role of diffraction in the resolution of an optical system is evident in several experiments. For instance, we have seen that when a wave encounters an object, it bends around its edges because of diffraction. This suggests that it is difficult to produce a perfect image of a sharp edge. Similarly, when an optical system images a point light source, the outcome is not a sharp point but a blurred spot. Specifically, in microscopy, the image of a point source passing through the circular aperture of an objective lens produces a diffraction pattern with a bright central region and a series of concentric and alternating bright and dark rings, known as Airy disks. Figure 1.4A shows the 3D representation of an Airy pattern, known as the point spread function (PSF), which depends on the optics of the microscope and the wavelength of light.

If the two light points are far away one from each other, their PSFs do not overlap, and they are easy to recognize as separate entities. Nevertheless, as soon as the distance between two points reduces and their PSFs overlap, a limit is reached where it is no longer possible to resolve them. Several criteria exist to quantify this limit. Among others, the most famous and widely used is the Rayleigh criterion, which states that the resolution is the distance between PSFs producing an intensity dip of 26 %[4]. Figure 1.4B shows a graphical representation of this criterion. Using the Rayleigh criterion, the lateral resolution of a microscope can be computed as:

$$d_{xy} = 0.61 \frac{\lambda}{NA} \tag{1.8}$$

where NA is the numerical aperture of the objective lens calculated as $NA = n \sin(\theta)$, with θ being the half-angle of the cone of light collected by the lens and n the refractive index of the medium between the sample and the lens.
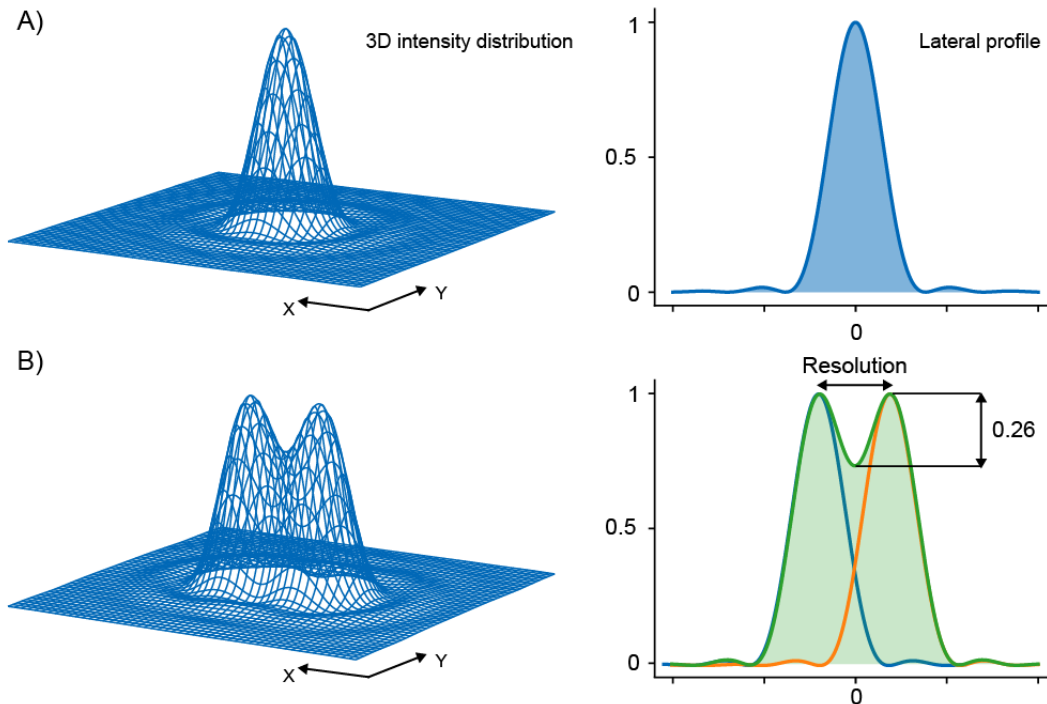

Figure 1.4. (A) Point spread function, 3D intensity, and lateral intensity profile for a diffraction-limited circular lens. (B) Resolution limit according to the Rayleigh criterion. The superimposed PSFs display two maxima separated by a valley. The intensity in the valley is ~26% compared with the two maxima.

Similarly, diffraction poses a limit also in the axial resolution, namely the minimum distance between two resolvable entities along the z-axis, given by the following equation:

$$d_z = n \; \frac{\lambda}{NA^2} \tag{1.9}$$

For instance, for an optical microscope equipped with an objective lens with a numerical aperture of 1.40, the theoretical resolution limit at the shortest practical visible wavelength, let's say 400 nm, is ~150 nm in the lateral dimension and 400 nm in the axial dimension. Even though the spatial resolution is intrinsically limited by diffraction, the optical microscope is still a fundamental tool for studying a wide range of samples in many fields as important as molecular and cellular biology.

1.2.2 Contrast

Together with the resolution, the image contrast is another key element of any microscopy technique. This corresponds to the ability of a "detail" of an image to stand out against the background or other neighboring details. To put it simply, the contrast makes visible the individual features of a specimen. From a mathematical point of view, the image contrast C can be calculated as:

$$C = \frac{I_S - I_B}{I_S + I_B} \tag{1.10}$$

where I_B is the intensity of the background and I_S that of the specimen. The specimen contrast is particularly important when working with biological samples such as cells. These samples are almost transparent in the visible because their effective refractive index only slightly differs from that of their surroundings; as both mainly consist of water. In order to image biological samples, it is, therefore, necessary to increase the specimen contrast. This is possible because contrast is not an intrinsic property of the specimen but depends on its interaction with the probing light. As a matter of fact, sufficient contrast can be produced in the specimen by exploiting light absorption[5], polarization[6], and scattering[7] as well as fluorescence[8] and phase variations[9]. The choice of a method depends on the requirements of a specific application and the optical properties of the specimen. For instance, samples that absorb light can be imaged with sufficient contrast by using a conventional brightfield microscope.

For weakly absorbing samples, fluorescence is the most used method because it provides contrast and specificity simultaneously[10]. In fluorescent microscopy, chemical labels (i.e., fluorescent molecules) bind to specific structures of the specimen and emit fluorescence when illuminated by light with proper energy. The emitted light has a wavelength lower than that of the excitation. The labels or fluorophores can be either organic or synthetic compounds[11]. Unfortunately, the labeling usually involves procedures (e.g., fixation) incompatible with live-cell imaging. Another problem is the risk of photobleaching, namely, a photochemical alteration of the fluorophore that inhibits its fluorescence. Photobleaching is caused by either high-intensity illumination or prolonged light exposure. A side effect of photobleaching is phototoxicity, i.e., the production of free radicals that damage subcellular components or cause cellular apoptosis. Although fluorescence microscopy is considered the standard for biological studies, all the above-mentioned issues have driven the development of label-free techniques in which the specimen contrast is produced without using fluorescent markers. Among others, phase contrast microscopy is emerging as a valid label-free method for studying biological samples. Details of phase contrast microscopy are presented next; readers interested in other label-free contrast methods can refer to recent review papers on this subject[12-13-14].

1.2.3 Phase Contrast Microscopy

In physics, the so-called "*phase problem*" denotes the loss of phase information that occurs during an optical measurement with standard light sensitive devices, such as CMOS or CCD cameras or photosensitive films, which cannot follow the oscillation rate of the electromagnetic waves, 10^{15} Hz or higher[15]. Indeed, these detection systems measure the photon flux, which is only proportional to the magnitude squared of the electromagnetic field, not its phase. Consequently, measuring the phase of optical waves needs additional complexity, typically using interference with a reference wave. Regardless of the specific implementation, interferometric imaging systems exploit the same strategy to recover the phase information of light waves, namely, the phase shift is converted into an amplitude signal and, hence, pixel values of an image. Some of these techniques, such as phase-contrast microscopy[16], provide semi-quantitative results, others such as holography[17], can be quantitative.

The first phase-contrast (PC) microscope was invented in the early 1930s by Frits Zernike[16]. In this microscope, two elements influence the specimen contrast: 1) the light scattered by the sample, and 2) the fraction of illuminating light that is not perturbed (background light). After probing the sample, the phase difference between these two contributions is eliminated with a phase-shift ring (component made of a material that dims the light passing through it and changes its phase by λ/n). In this way, when focused on the image plane (where the camera or eyepiece is placed), background and scattered light constructively interfere, resulting in an increase in the brightness of sample areas probed by the light. This method was initially used to characterize a coarse and transparent grating (phase grating) with shallow grooves and later applied to the inspection of objects with arbitrary shapes. In particular, Zernike proved that transparent objects with a variable thickness or refractive index produce measurable intensities in the image[16]. The technique was particularly important in the field of biology because it allowed specific details of cells, which were otherwise transparent to a brightfield microscope, to be revealed. The pioneering work of Zernike opened up the way to the development of novel contrast-enhancing techniques based on phase variation. In particular, Differential Interference Contrast microscopy (DIC), developed by physicist Georges Nomarski in 1952, showed some clear advantages with respect to traditional PC. The operational principle consists of separating polarized light into two perpendicularly polarized components. These two are spatially displaced at the sample plane and then recombined before observation. The interference of the two parts is sensitive to the optical path difference, which is due to the difference in refractive index and path length they experience while traveling through the sample. In other words, DIC is an interferometric method where the specimen contrast is proportional to the path length in the direction of the two probing beams[18].

Traditional phase-contrast methods surely represent valid tools to image transparent specimens, such as living cells, without the use of dye/labels and excessive sample manipulations (Figure 1.5A). Nevertheless, a problem exists with PC and DIC images since they do not provide quantitative measures of the phase differences (Figure 1.5B). To overcome these limitations, Quantitative Phase Imaging (QPI) approaches soon developed[19] (Figure 1.5C). QPI combines different techniques (microscopy, holography, and scattering) to quantify the extent of phase delay introduced by the sample and record it as pixel values within the generated image.
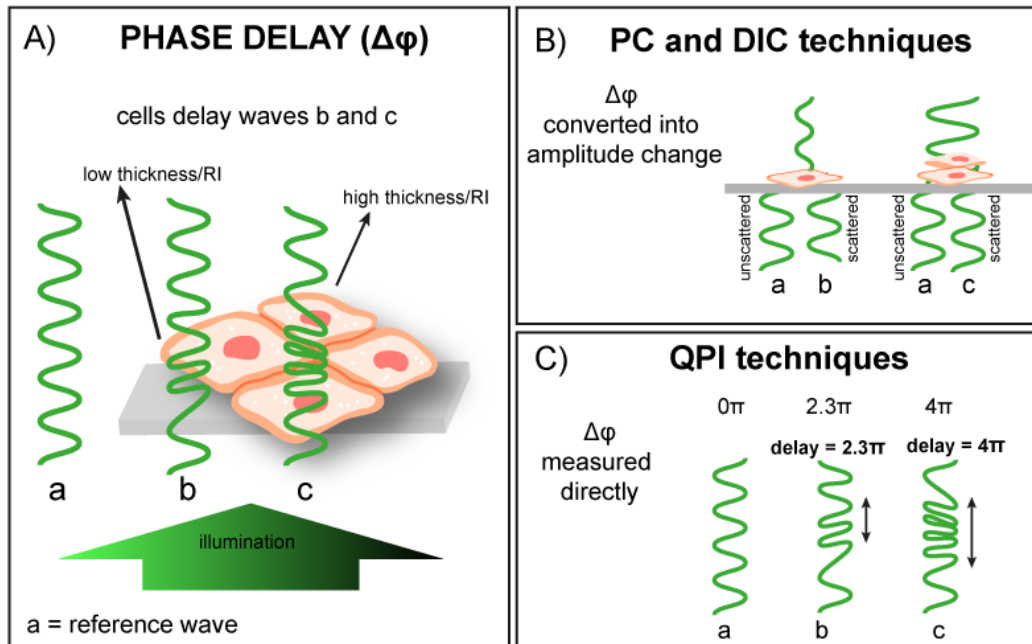
Figure 1.5. Phase delay as sample contrast. A) Phase delay (Δφ) introduced by cells, where "a" is the unperturbed reference wave, "b" and "c" are delayed depending on the thickness and/or refractive index of the sample. B) Qualitative PC and DIC measure the phase delay as amplitude of the exit waves. C) QPI techniques directly measure the phase delay as pixel intensity.

Among QPI techniques, we can find various holographic microscopy methods and, in particular, Ptychography.

1.3 Ptychography

Ptychography was invented in 1970 in the context of crystallography by Hegerl and Hoppe, which also named the technique[20]. The word "Ptychography" derives from the Greek "*ptycho*", meaning "*to fold*," indicating that the waves scattered by a sample "fold" into one another. Ptychography is a scanning-based coherent diffractive imaging technique, which is able to generate images by processing several *coherent* diffraction patterns scattered by the sample. Since the collected patterns *encode* the information we are interested in, ptychography uses our

mathematical understanding of light-matter interactions to *decode* them and retrieve both the amplitude and the phase of the scattered wavefield[15].

The open question is how does ptychography solve the "phase problem"? To answer this question, let us consider the simplest configuration of a ptychography microscope: a source of light waves traveling first through an aperture and then the sample of interest. The exit waves resulting from this interaction are recorded with a camera, which stands at a certain distance from the sample. To measure their amplitude and phase and, thus, characterize in detail the sample, multiple diffraction patterns are generated and processed with an iterative algorithm; the most common is the extended Ptychographic Iterative Engine (ePIE). Figure 1.6 shows a schematic description of the operations needed to solve the phase problem in ptychography. Details about the images reconstruction process will follow in Chapter 2. The general idea is that the algorithm iteratively performs inverse calculations based on Fourier optics and applies some constraints (the recorded data) to compute amplitude and phase of the optical field everywhere between the illumination and the detector, including the sample plane. To ensure the uniqueness of the reconstructed field, the phase problem is over-constrained, meaning that the specimen is scanned with an array of overlapping illuminated areas.
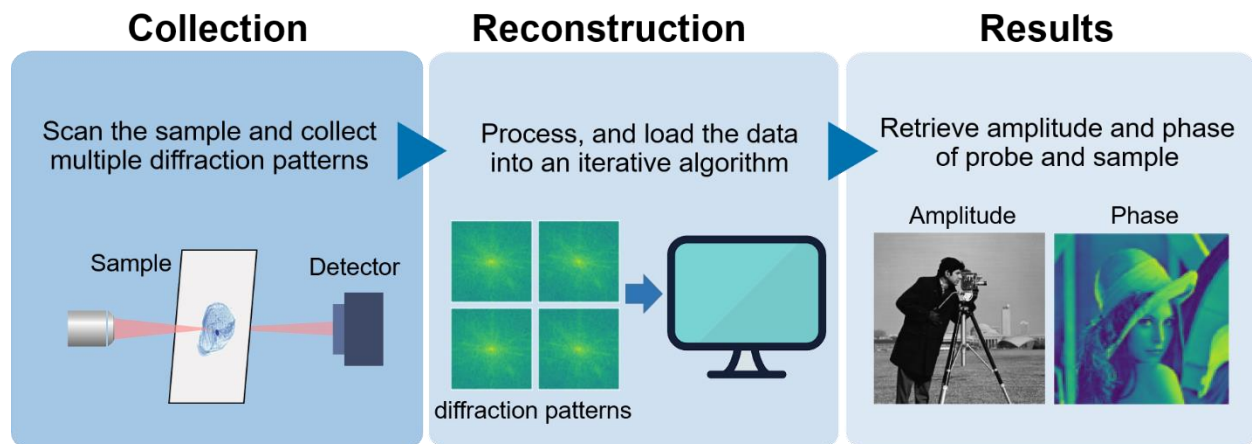
Figure 1.6. Schematic description of a ptychography experiment. Starting from the left box, we have the sample of interest illuminated with our probe in multiple positions overlapped; from each of these positions, a minimum of one diffraction pattern is registered on the detector. All the diffraction patterns are processed and then analyzed using an iterative reconstruction algorithm (middle box) that, after several iterations is able to retrieve the phase and amplitude of our sample (right box).

Therefore, unlike standard interferometric imaging methods, such as holography, ptychography reconstructs the phase and amplitude of a scattered wavefield without the need of a reference wave[21]. Even if this ability has a significant computational cost, the hardware requirements for implementing ptychography can be extremely simple. The fundamental components are: 1) a light probe, 2) a scanning system, and 3) a camera. From this description, it is clear the simplicity of the technique that makes ptychography cost-effective and simple to implement on standard microscopes.

Another value of ptychography is its versatility. Even if it was originally proposed as a lensless approach (Figure 1.7A), with the aim of avoiding the aberrations caused by curved lenses[22], novel configurations that exploit lenses or microscope objectives have been also reported[23]. At the cost of increased system complexity, this solution provides some benefits, including a more reliable image reconstruction and improved spatial resolution[23]. Representative examples of lens-based ptychographic systems are the so-called "*microscope setup*" and the "*selected area setup*" (Figure 1.7B and C). In the first implementation, the detector on top of the sample is replaced with a virtual detector plane; in the other setup, a microscope is used to image the sample and a pinhole to shape the probe. By increasing a bit more the system complexity, ptychography can achieve 3D imaging capabilities via the multi-slice method[24] or in combination with tomography[25]. It has been also modified to operate in a Bragg geometry[26] and adapted to eliminate the mechanical scan via Fourier Ptychography[27], where the scanning is carried out by illumination tilts.
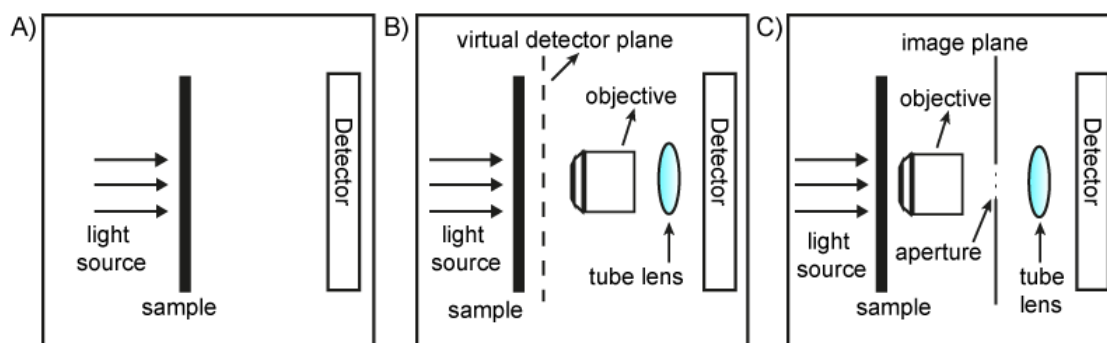

Figure 1.7. Three different experimental configurations of ptychography. A) Lensless setup, where there are no lenses in between the specimen and the detector. B) Microscope setup, where the detector is replaced with its demagnified image. C) Selected area setup, where the object is moved relative to a selected area aperture placed in the image plane of the objective lens.

The versatility of ptychography is also evident from the wide range of compatible wavelengths. As a matter of fact, it has been applied to electron, X-ray, and optical microscopy[28-29]. The application of Ptychography to electron microscopy can be dated back to the late '90s when Nellist et al. demonstrated an aberration-free image of crystalline silicon that resolved its atomic spacing (~ 0.136 nm)[30]. More recently, Chen et al. pushed this limit, reaching a lateral resolution comparable with the thermal vibration of the atoms in a crystal, thus demonstrating that is theoretically possible to identify a single atom in a bulk material[31]. Also, in the X-ray regime, ptychography has reached a nanometric resolution. Precisely, X-ray ptychography has been successfully used to characterize the focusing properties of X-ray optics[32], microchips[33], and to image yeast cells with a resolution as low as 15 nm[34]. Although the impressive resolution they provide, electron beams and X-rays do not always represent the best choice for studying biological samples. First of all, to be imaged with these radiations, biological samples need specific and invasive treatments that cause the death of the cells. Furthermore, the sample irradiated with electrons and X-rays cannot be reused for multiple or recursive analyses. For this reason, we focused this thesis on the application of ptychography to visible wavelengths. In this regime, ptychography allows the label-free imaging of biological samples either *in vitro* or *in vivo*, without the need for cytotoxic chemicals (Figure 1.8). For instance, optical ptychography can discriminate cellular changes (e.g., mitosis, apoptosis, and cell differentiation)[21] and even distinguish quantitatively between healthy and tumorous unstained cells[35]. Recently, Anthony et al. demonstrated that optical ptychography can identify cell death much earlier than a comparative fluorescence study, providing new insights into the changes that occur during the cell cycle[36]. All the above results indicate the potential of optical ptychography as a tool for studying biological processes. Nowadays, several works, including this thesis, aim at making optical ptychography competitive with modern fluorescence microscopy techniques or complementing them with label-free operations[37-38].
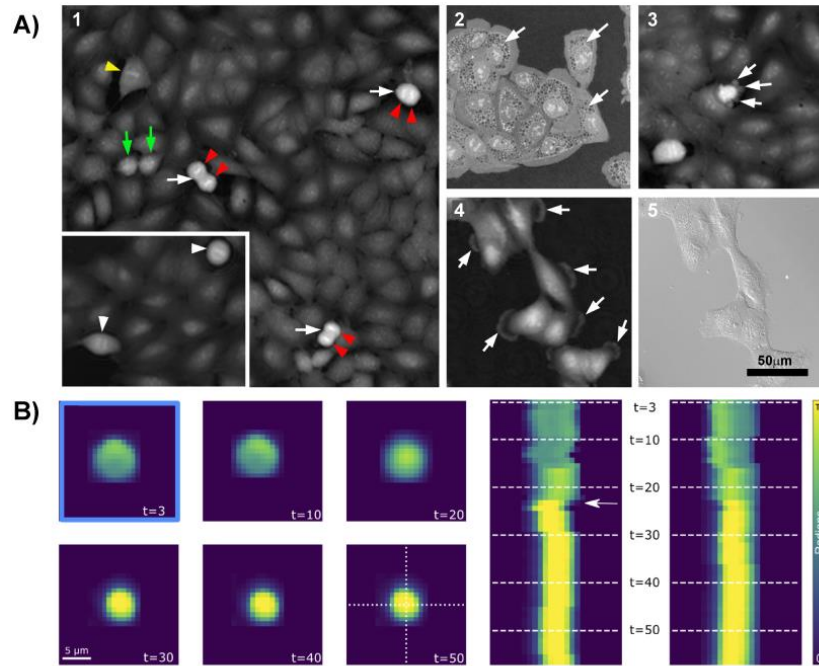
Figure 1.8. Optical Ptychography measurements for the identification of cellular changes. A) Starting from (1) is possible to see actively dividing cells (arrows); (2) vesiculation of the cytoplasm due to heat shock (arrows); (3) apoptotic cell with membrane blebbing; (4) cells in a non-confluent preparation showing membrane ruffles. (5) DIC image of the same field of view as (4) where membrane ruffles are barely visible[21]. B) Evolution of the phase distribution for a single cell that undergoes apoptosis at 6 different time points (i.e., 3, 10, 20, 30, 40, 50 minutes). Horizontal and vertical slices of the phase distribution are also reported[36].

Bibliography

1.   Greiner, W. *Quantum Mechanics: An Introduction*. (Springer US, 2011).

2.   Carlsson, K. Imaging physics. *X-ray Microsc.* 71–198 (2019). doi:10.1017/9781139924542.005

3.   Porter, J. R. Antony Van Leeuwenhoek. Tercentenary of his discovery of bacteria. *Bacteriol. Rev.* **40**, 260–269 (1976).

4.   Jelley, E. E. Light microscopy. *Anal. Chem.* **21**, 40–44 (1949).

5.   Jafari, M., Guo, L. J. & Rais-Zadeh, M. An ultra-fast optical shutter exploiting total light absorption in a phase change material. in *Optical Components and Materials XIV* (eds. Jiang, S. & Digonnet, M. J. F.) **10100**, 89–95 (SPIE, 2017).

6.   Le Gratiet, A. *et al.* Zebrafish structural development in Mueller-matrix scanning microscopy. *Sci. Rep.* **9**, 19974 (2019).

7.   Gratiet, A. Le *et al.* Circular intensity differential scattering (CIDS) scanning microscopy to image chromatin-DNA nuclear organization. *OSA Contin.* **1**, 1068–1078 (2018).

8.   Lanzanò, L. *et al.* Measurement of nanoscale three-dimensional diffusion in the interior of living cells by STED-FCS. *Nat. Commun.* **8**, 65 (2017).

9.   Balaur, E. *et al.* Plasmon-induced enhancement of ptychographic phase microscopy via sub-surface nanoaperture arrays. *Nat. Photonics* **15**, 222–229 (2021).

10.   Kasprowicz, R., Suman, R. & O'Toole, P. Characterising live cell behaviour: Traditional label-free and quantitative phase imaging approaches. *Int. J. Biochem. Cell Biol.* **84**, 89–95 (2017).

11.   Zanacchi, F. C. *et al.* A DNA origami platform for quantifying protein copy number in super-resolution. *Nat. Methods* **14**, 789–792 (2017).

12.   Kim, M. K. Principles and techniques of digital holographic microscopy. *SPIE Rev.* **1**, (2010).

13.   Le Gratiet, A., Mohebi, A., Callegari, F., Bianchini, P. & Diaspro, A. Review on Complete Mueller Matrix Optical Scanning Microscopy Imaging. *Appl. Sci.* **11**, (2021).

14.   Le Gratiet, A., Marongiu, R. & Diaspro, A. Circular Intensity Differential Scattering for Label-Free Chromatin Characterization: A Review for Optical Microscopy. *Polymers*

(Basel). **12**, (2020).

15. Rodenburg, J. & Maiden, A. *Ptychography*. (2019).

16. Zernike, F. Phase contrast, a new method for the microscopic observation of transparent objects part II. *Physica* **9**, 974–986 (1942).

17. Shechtman, Y., Eldar, Y. C., Cohen, O. & Chapman, H. N. with Application to Optical Imaging. 87–109 doi:10.1109/MSP.2014.2352673

18. Chehab, F. F., Lim, M. E. & Lu, R. Correction of the sterility defect in homozygous obese female mice by treatment with the human recombinant leptin. *Nat. Genet.* **12**, 318–320 (1996).

19. Park, Y. K., Depeursinge, C. & Popescu, G. Quantitative phase imaging in biomedicine. *Nat. Photonics* **12**, 578–589 (2018).

20. Hegerl, R. & Hoppe, W. Dynamische Theorie der Kristallstrukturanalyse durch Elektronenbeugung im inhomogenen Primärstrahlwellenfeld. *Berichte der Bunsengesellschaft für Phys. Chemie* **74**, 1148–1154 (1970).

21. Marrison, J., Räty, L., Marriott, P. & O'Toole, P. Ptychography-a label free, high-contrast imaging technique for live cells using quantitative phase information. *Sci. Rep.* **3**, 1–7 (2013).

22. Thibault, P. *et al.* High-Resolution Scanning X-ray Diffraction Microscopy. *Science (80-.).* **321**, 379–382 (2008).

23. Hang, H. E. Z. *et al.* Near-field Fourier ptychography : super- resolution phase retrieval via speckle illumination.

24. Maiden, A. M., Humphry, M. J. & Rodenburg, J. M. Ptychographic transmission microscopy in three dimensions using a multi-slice approach. **29**, 1606–1614 (2012).

25. Dierolf, M. *et al.* Ptychographic X-ray computed tomography at the nanoscale. *Nature* **467**, 436–439 (2010).

26. Godard, P. *et al.* Three-dimensional high-resolution quantitative microscopy of extended crystals. *Nat. Commun.* **2**, 568 (2011).

27. Zheng, G., Horstmeyer, R. & Yang, C. Wide-field, high-resolution Fourier ptychographic microscopy. *Nat. Photonics* **7**, 739–745 (2013).

28. Takahashi, Y. *et al.* Towards high-resolution ptychographic x-ray diffraction microscopy.

214109, 1–5 (2011).

29.   Chalkidis, S. X-ray and Visible Light Near-field Ptychography. (2015).

30.   Nellist, P. D., McCallum, B. C. & Rodenburg, J. M. Resolution beyond the 'information limit' in transmission electron microscopy. *Nature* **374**, 630–632 (1995).

31.   Chen, Z. *et al.* Limits Set By Lattice Vibrations. *Science (80-.).* **372**, 826–831 (2021).

32.   Schropp, A. *et al.* Hard x-ray nanobeam characterization by coherent diffraction microscopy. *Appl. Phys. Lett.* **96**, 91102 (2010).

33.   Schropp, A. *et al.* Non-destructive and quantitative imaging of a nano-structured microchip by ptychographic hard X-ray scanning microscopy. *J. Microsc.* **241**, 9–12 (2011).

34.   Giewekemeyera, K. *et al.* Quantitative biological imaging by ptychographic x-ray diffraction microscopy. *Proc. Natl. Acad. Sci. U. S. A.* **107**, 529–534 (2010).

35.   Claus, D. *et al.* Quantitative phase contrast optimised cancerous cell differentiation via ptychography. *Opt. Express* **20**, 9911 (2012).

36.   Anthony, N. *et al.* Ptychographic imaging of NaD1 induced yeast cell death. *Biomed. Opt. Express* **10**, 4964 (2019).

37.   Wu, J. *et al.* Super-resolution fluorescence blinking imaging using modified Fourier ptychography. *Opt. Express* **26**, 2740 (2018).

38.   Dong, S., Nanda, P., Shiradkar, R., Guo, K. & Zheng, G. High-resolution fluorescence imaging via pattern-illuminated Fourier ptychography. *Opt. Express* **22**, 20856 (2014).

2 The ptychographic microscope

2.1 Introduction

In this work, among the possible ptychographic architectures, we focused our attention on the so-called ptychographic microscope setup (section 1.3). This design not only allows increasing the signal measured by the camera but also to fully exploit its dynamic range, namely, the ratio between the maximum output signal and the noise level when the detector is kept in the darkness. As such, we believe that this choice is particularly suitable for imaging biological cells, which weakly scatter light because of the modest refractive index contrast between their subcellular entities. This chapter is organized as follows: first we will detail the hardware elements of the microscope (section 2.2) and the software developed for amplitude and phase recovery (section 2.3). In section 2.4 we will show the successful application of the ptychographic microscope to the imaging of representative organic and inorganic samples, and finally, in section 2.5, we will report on the characterization of essential microscope parameters such as field of view, spatial resolution, and image contrast.

2.2 Microscope design

In the microscope setup, the detector is placed on top of the sample, not physically as for the lensless setup configuration (Figure 1.7A), but by means of a 4f system or telescope comprising a tube lens and an objective lens. This produces a demagnified image of the detector at the focal point of the objective, which we named the "virtual detector plane". Because this magnification produces a detector that is smaller compared to the lensless setup, the distance from the specimen

to the virtual detector plane can be selected to avoid the loss of photons scattered beyond the edges of the active area of the detector. The microscope setup not only increases the signal measured by the detector but also fully exploits its dynamic range. As a matter of fact, since the virtual detector plane is so close to the sample plane, the resulting diffraction patterns have narrower dynamic ranges, which places them within the dynamic range of the detector. We can say that the main limitation for this setup is the use of good quality and high NA objectives lens.

Concerning the data collection, this was performed using Fermat spiral patterns[1]. This pattern is very useful for ptychography, where two conditions are fundamental to achieve artefact-free images: 1) breaking the translational symmetry of the scan pattern and 2) achieving a uniform overlap between points. The spiral reduces the risk of introducing these possible artifacts, and it also speeds up the acquisition with respect to a classic raster scan, which is well-known for introducing such artifacts[2]. Data were analyzed using a Python software developed for fast and efficient recovery of phase and amplitude images[3].

2.3 Hardware

Figure 2.1 shows a schematic description of our ptychographic microscope. The key element of the setup is a pair of microscope objectives. The lower (illumination) objective is used to shed light onto the sample, and the upper (collection) objective to collect the light transmitted through or scattered by the sample. Hereafter, for simplicity, we will refer to the lower objective's focal plane as the "objective plane".

In this work, we used two 20X microscope objectives (Nikon series) operating in air with numerical aperture NA=0.5 and working distance WD=2.1 (Plan Fluor, Nikon Inc.) for the collection and with NA= 0.7 and WD=1.0 (Plan Apo VC, Nikon Inc.) for the illumination.
The light source used was a fiber-coupled 561-nm-wavelength Sapphire continuous-wave laser (Coherent Sapphire 561-200 CW CDRH). The laser beam exiting the fiber is slightly diverging; therefore, we placed a plano-convex converging lens (Thorlabs, AC254-050-A-ML, f=50 mm) in order to collimate the beam. We used a shear plate (Thorlabs, SI254) to finely adjust the collimation of the beam, this latter depending on the distance between the lens and the fiber tip.
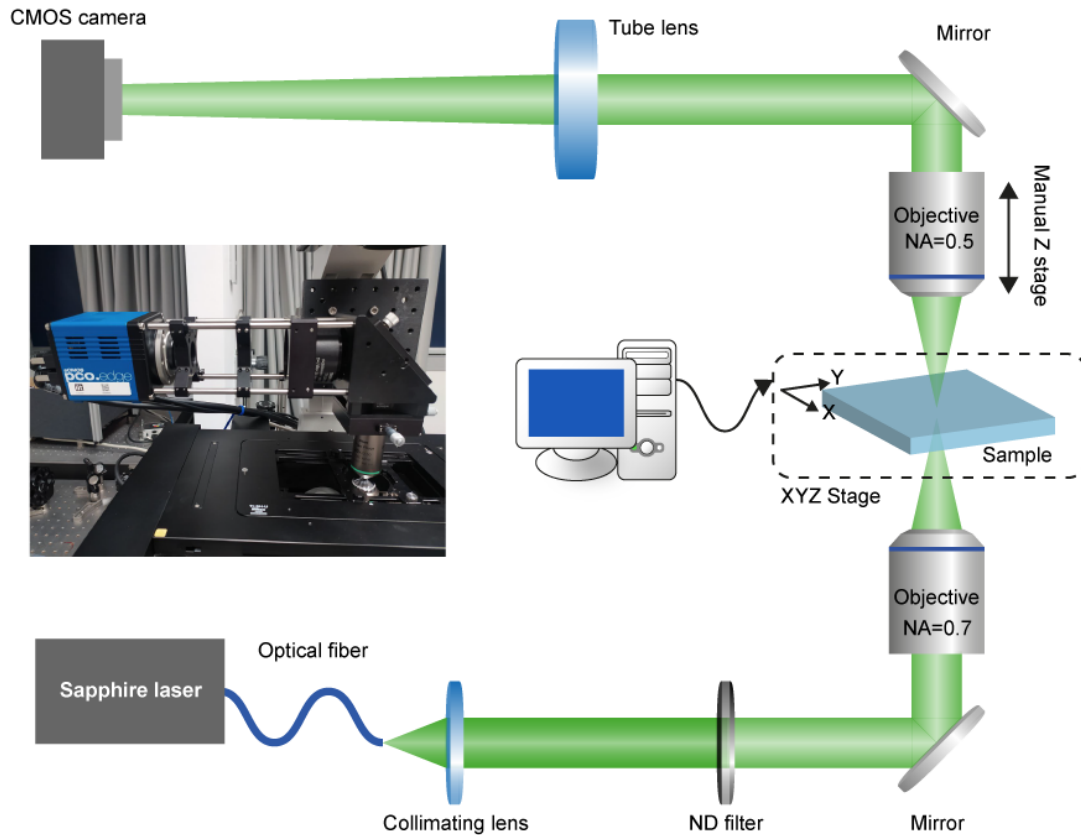
Figure. 2.1. Ptychography setup. Schematic representation of the optical components used in the illumination and detection parts of the microscope. A fiber collimated beam with wavelength 561 nm is filtered and focused on the sample through a 20X objective. After being scattered from the sample, the exit wave is collected from a 20X objective and focused onto the detector by a tube lens. The insert shows a picture of the detection arm.

We used a rotating wheel equipped with various neutral density filters (OD from 0.2 to 3.0) to adjust the intensity of the illumination according to the optical properties of the sample. Finally, by using silver mirrors, we precisely aligned the laser beam with the optical axes of the illumination objective. This collimated Gaussian beam fills the back-aperture of the illumination objective. Once the probe is focused on the sample, it is scattered, generating a diffraction pattern distinctive of the sample optical properties. This diffraction pattern is recorded with a scientific CMOS camera (Pco.edge 4.2, sCMOS) with 2048×2060 active pixels ($N_{pix} = 2048$) and pixel pitch (d_c) of 6.5 μm. We used a tube lens (Thorlabs, TTL-200A with a focal length of

200 mm) to focus the diffraction pattern, collected by the upper microscope objective, into the active area of the camera. The magnification M of the telescope consisting of the tube lens and the collection objective was 20. Notably, the collection objective, tube lens, and camera are integrated into a compact and lightweight module (inset of Figure 2.1), which can be easily mounted onto any commercial microscope. In this work, we integrated this module into a widefield microscope (Nikon, Eclipse Ti), taking benefit from all its functionalities and components, such as the XYZ sample stage, oculars, and sample holder.

2.4 Software

2.4.1 Data collection code

The data were collected and analyzed in Python (Python 3.7)[3]. Custom data collection code coordinates the microscope stage (Nikon, TI-SH-U) and the sCMOS camera using μManager[4]. The software controls the mechanical stage to move the sample with respect to the illumination according to a user-selectable scanning scheme. At each position, the camera is triggered to collect and save the data before moving to the next position. For each position scanned, we programmed an overlap of 80% between neighboring frames. This redundancy makes the iterative re-phasing algorithm more reliable and robust[5]. In this work, we scanned the sample with a Fermat spiral (Figure 2.2)[6]. The data collection code receives various inputs that can be used to optimize the acquisition. Among others, the most relevant are the number of positions (N_P), number of frames (N_F) for each position, exposure time (τ), sample-to-objective plane distance (Z_{24}), and sample-to-virtual detector plane distance (Z_{43}). A schematic representation of the two latter inputs is shown in Figure 2.3. Regarding the number of exposures and the exposure time, we calibrated them by taking into account the signal-to-noise ratio (SNR) and the saturation (dynamic range) of the detector. The strategies to increase the SNR are increasing the laser intensity and extending the exposure time. However, both solutions are limited by the detector saturation, namely the number of photons reaching the detector exceeds the maximum number of photons detectable by the detector's pixels. The sCMOS camera used for this work saturates at 65,000 counts. Moreover, extending the exposure time means that together with a higher signal, we are registering a higher level of noise.
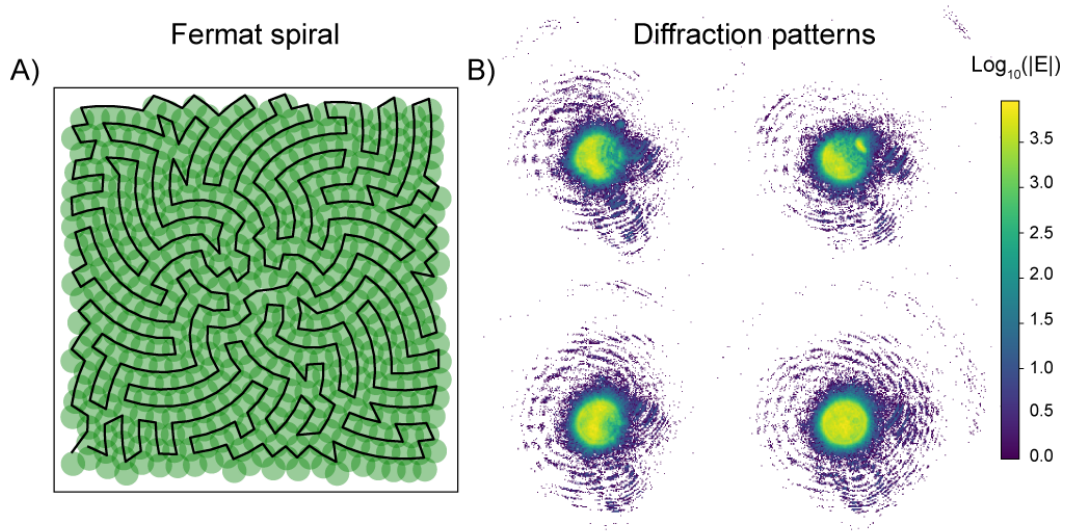
Figure 2.2. A) Concept of the Fermat spiral scanning. B) Four representative examples of collected diffraction patterns. The data are plotted on a logarithmic scale to better highlight patterns' features.
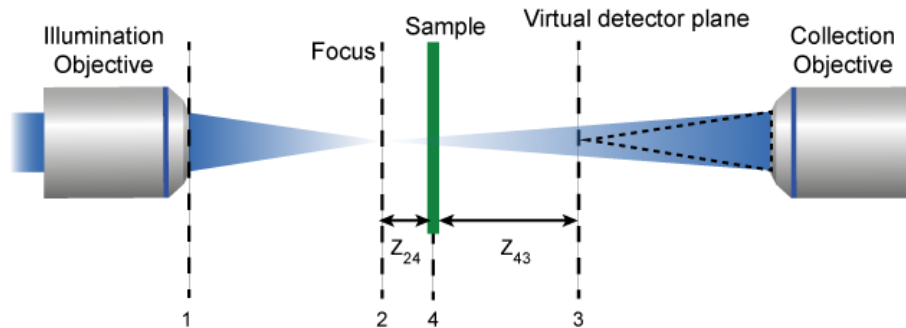

Figure 2.3. Ptychography system. The figure shows the core of the ptychographic imaging, with the two objectives (microscope objective and virtual detector plane) in line and the sample in between. Light propagates from left to right. Highlighted are the most relevant planes that define the distances set in the acquisition step. In particular, the distance between the focus of the objective and the sample Z_{24} and the one between the sample and the virtual detector plane Z_{43}.

To avoid saturation and reduce the noise, a practical solution is averaging over multiple frames acquired for each position with a short exposure time. In this work, we acquired between 3 and 5 frames for each scanned position and used an exposure time of 10 ms.

The distance between the objective plane and the sample is the parameter Z_{24} that, together with the objective NA, defines the size of the probe (W) according to the following equation:

$$W = Z_{24}tan(asin(NA)) \tag{2.1}$$

Probe size, number of positions, and probe overlap determine the step size (ΔS) of the scan and, thus, the field of view (FOV) of the ptychographic microscope as follows:

$$\Delta S = W * (1 - overlap) \tag{2.2a}$$

$$FOV = \left(\sqrt{N_P} - 2\right)\Delta S \tag{2.2b}$$

Figure 2.4A shows the expected field of view of our ptychographic microscope as a function of the distance from the focus to the sample (Z_{24}) and for a Fermat spiral with a number of positions N_P from 64 to 2048. For the hardware configuration in this work, we can clearly cover a FOV of several tens of microns, which is enough for studying biological samples such as living cells. The distance between the sample and the virtual detector plane Z_{43}, along with the number of positions N_P and the pixel size of the virtual detector d_V determine the pixel size (d_I) of the reconstructed image according to the following equations:

$$d_V = 2 * d_C/M \tag{2.3a}$$

$$d_I = \lambda\, Z_{43}/(N_{pixel}\, d_V) \tag{2.3b}$$

As shown in Figure 2.4B, a higher distance between the virtual detector and the sample reduces the d_I value. However, within the Z_{43} range of this thesis, we are still theoretically able to reconstruct images with sub-micrometric pixel size.

At the end of the scan, all the diffraction patterns are stored in a compressed .hdf5[7] Hierarchical Data Format file together with darkfield data (i.e., image without illumination) and whitefield data (i.e., illumination without sample). HDF5 files were used because they are compressible without reducing the quality of the data. Compression of the data is useful to reduce their overall size and save memory on the disk. This is an important aspect to consider for ptychography, which requires large quantities of data and, thus, significant storage and analysis capabilities. As detailed next, following the collection steps, the data are analyzed using three different Python codes: the data processing code, whitefield reconstruction code, and extended ptychographical iterative engine (ePIE).
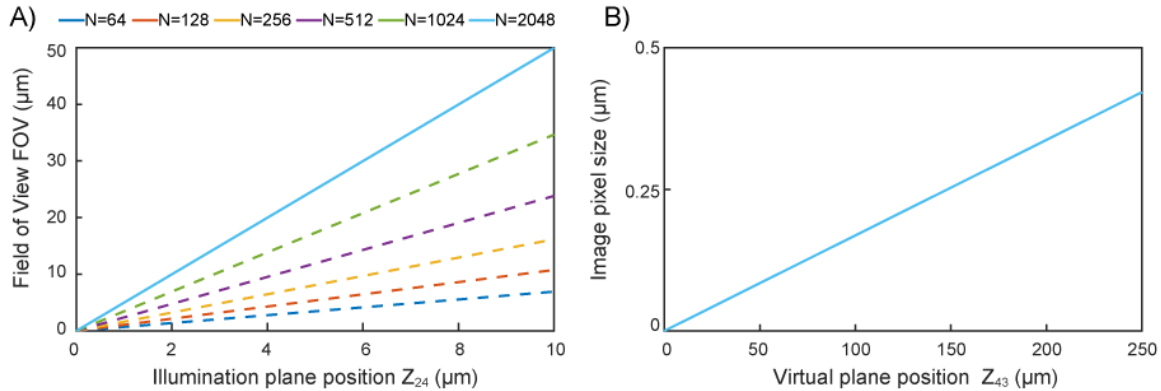
Figure 2.4. A) Calculated field of view for various Z_{24} values and for a scanning scheme with N_P ranging from 64 to 2048. B) Image pixel size vs. Z_{43} values. Calculations were performed for λ=541 nm, NA=0.7, and NA=0.5 for the illumination and collection objectives, respectively. The overlap between two consecutive scanned areas was 80%. The continuous blue line denotes the parameter options most used in our experiments.

2.4.2 Data process code

First, the data are processed using the recorded whitefield (WF) and darkfield (DF) images. The sequence of operations needed to process the recorded data is summarized in the block diagram of Figure 2.5. Briefly, the Python routine subtracts the DF, which corresponds to the background noise of the detector, from the collected frames and applies an intensity threshold. The threshold is computed for each frame by averaging a region of interest in the WF dataset. This step is independently performed for all the exposures for each position of the scan. The averaging procedure aims at "cleaning" the raw data from extraneous values and preparing them for the next processing steps. Relevant parameters for performing a correct data processing are the rebinning factor (BF), padding factor (PF), and the threshold intensity (I_{Th}). The "binning" process consists of assigning to each pixel of an image the sum of the adjacent ones. This reduces the size of the image and, thus, increases the speed of the reconstruction, though, it also leads to a loss of resolution determined by the number of pixels merged (see equations 2.3). In this work, we found that a binning factor of 2 results in good reconstructed images without requiring excessive reconstruction times.
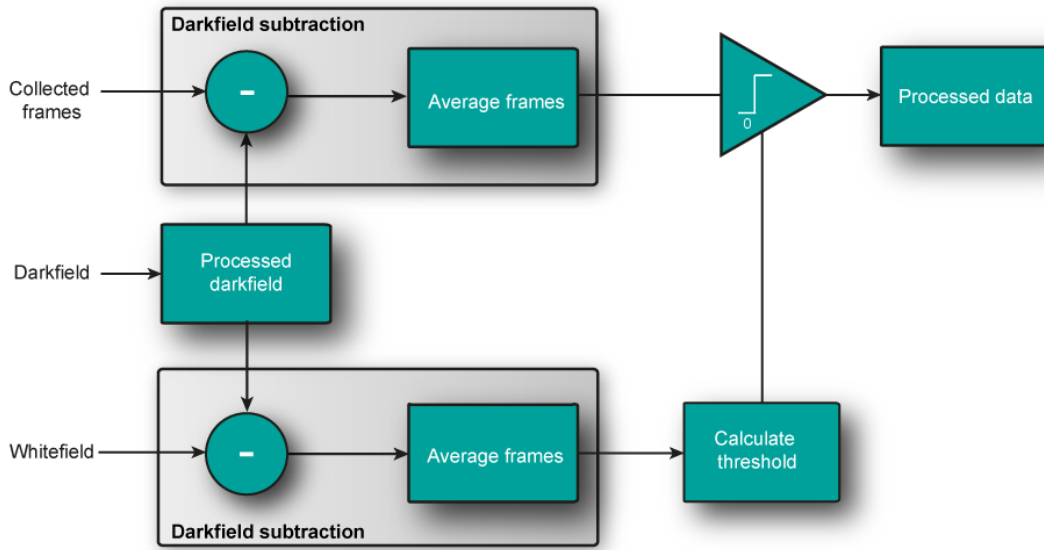
Figure 2.5. Block diagram describing the operational principle of the data processing code. The input received are: darkfield, whitefield, and the collected frames. After the darkfield subtraction, the whitefield is used to calculate a threshold and in turn to filter the data.

 "Padding" adds space between the image and its border to increase the overall number of pixels and is useful for reducing the representative size of the pixels for a smoother final image. Although padding is possible, it was not used in this work. The rebin and padding factors must always be the same between the data processing, whitefield reconstruction, and ePIE.

2.4.3 Whitefield reconstruction code

This code reconstructs the phase of the collected WF by solving the propagation of the electric field from the illumination objective to the collection objective. To this end, a complete description of the electric field is needed, namely, its amplitude and phase. However, because of the phase problem (see Chapter 1), the phase and amplitude of the electromagnetic field cannot be imaged by means of intensity measuring detectors (sCMOS). We can overcome this problem by exploiting the information that the ptychographic microscope provides, namely, the amplitude of the field recorded by the detector and the amplitude of the beam entering the illumination objective. The reconstruction of the WF, therefore, works as follows. A Python program 1)

makes use of the processed WF data to generate a model, or a guess, of the wavefront of the field at the virtual detector and entrance of the illumination objective[8]. 2) It assumes an initial flat phase for both fields, and 3) computes the phase transformation due to light propagation between the objective and the detector, and vice-versa. After each step, the guessed amplitude of the electric field is imposed to be the measured one. This operation is iterated multiple times, and at each cycle, the phase, created by simulating the field propagation and imposing the constraints, is gradually refined until it converges to an amplitude and hence phase consistent with the experimental data. Once the missing phase information has been obtained, the wavefront can be calculated in any plane between the illumination plane and the virtual detector plane and, more importantly, to the plane of the sample.

2.4.4 Extended Ptychographic Iterative Engine (ePIE)

Many strategies have been developed to retrieve the phase of Ptychographic experiments. The task of any ptychographic algorithm is to calculate the correct phases for each diffraction pattern and, via an inverse Fourier transformation, recover the amplitude and phase of the sample. The most common algorithm for this task is the ptychographic iterative engine (PIE)[9] and its 'extended' version, the ePIE[8]. A flowchart describing the operations that ePIE performs to solve the phase problem is presented in Figure 2.6. Briefly, the elements to consider are a number J of collected diffraction patterns $I_j(\boldsymbol{u})$, with u being the coordinate of the pixels of each diffraction pattern, the XY positions on the sample plane $R_j = (x_j, y_j)$, the probe P_{0r} with r being the index of the pixels of the probe image, and the object O_{0x} with x being the index of the pixels of the sample image. ePIE starts with initial guesses, a random array for the object and a free-space propagation of the wave for the probe. As ePIE iterates, both the probe and the object arrays are updated to form images of the sample and probe. The first step of the ePIE algorithm is to update the initial probe guess from the WF reconstruction code, and the object guess using the collected diffraction patterns. The diffraction patterns are randomly selected through the index $S(j)$. Starting from j=1, ePIE calculates the exit-wave obtained by multiplying the object guess and the shifted probe guess:

$$\psi_j(\boldsymbol{r}) = P_j(\boldsymbol{r} - R_j)O_j(\boldsymbol{r}) \tag{2.4}$$

This is propagated toward the detector using a Fourier transform F, and then the modulus is replaced with the amplitude collected experimentally $I_j(\boldsymbol{u})$ so that

$$\Psi_j'(\boldsymbol{u}) = \sqrt{I_j(\boldsymbol{u})}\,\frac{\mathcal{F}[\psi_j(r)]}{|\mathcal{F}[\psi_j(r)]|} \tag{2.5}$$

The updated exit-wave is now calculated with inverse Fourier transform F^{-1}:

$$\psi_j'(\boldsymbol{r}) = \mathcal{F}^{-1}\big[\Psi_j(\boldsymbol{u})\big] \tag{2.6}$$
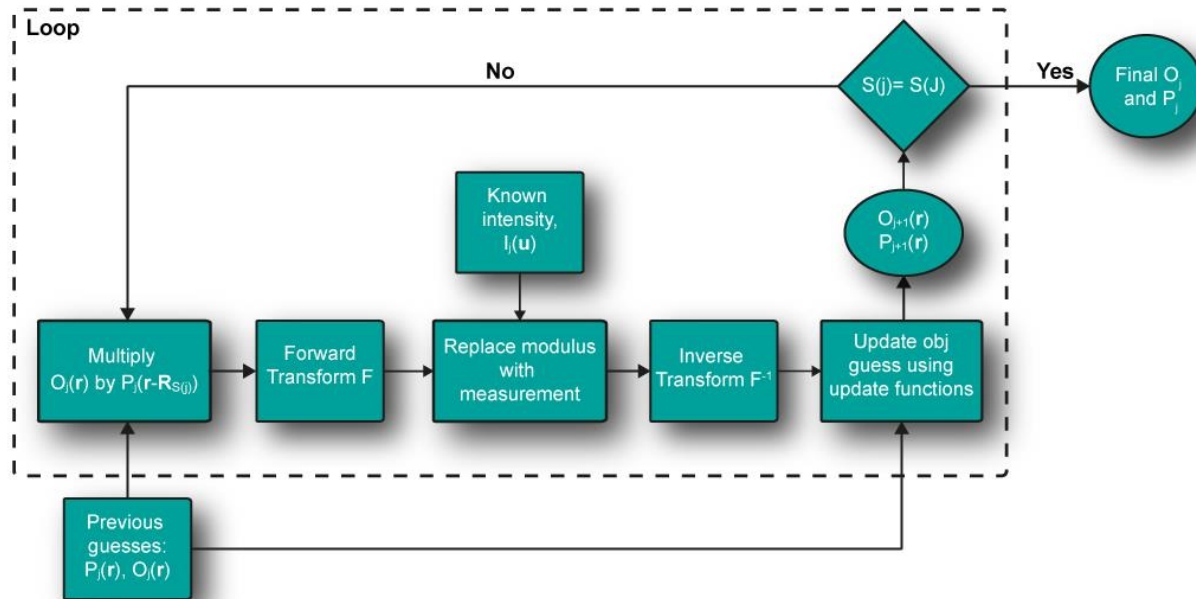

Figure 2.6. Flowchart of the ePIE method. At j = 0, initial guesses for both the sample $O_j(\mathbf{r})$ and probe $P_j(\mathbf{r})$ waveforms are provided to the algorithm. A guess of the exit wave is calculated by multiplying the current object guess by the appropriately shifted probe guess $P_j(\mathbf{r}\text{-}\mathbf{R}_{S(J)})$. A Fourier transform $\mathcal{F}$ is used to propagate the exit wave to the detector, where the measured intensity $I_j(\mathbf{u})$ is applied. After using an inverse Fourier transform $\mathcal{F}^{-1}$, we can recover the amplitude and phase of each exit wave, used to update the initial object and probe with the correspondent update functions. The dashed line identifies the iterative loop used for updating both object and probe. The loop repeats for every diffraction pattern S(j) until each of the *J* diffraction patterns has been used to update the object and probe guesses.

Following these operations, the algorithm extracts two updated functions, namely, the object and the probe. This process continues operating over the other diffraction patterns $S(1), S(2), S(3) \dots, S(J)$ until each of the J recorded frames have been used to update the object and probe guesses. At this point, a single ePIE iteration has been completed. This process repeats until the object and probe guesses are converged.

The quality of the reconstructed images strongly depends on the number of iterations. Unfortunately, there are no rules about the minimum value of N that ensures high-quality reconstructions; we cannot select it *a priori*. As detailed next, an experimental study is needed to determine the optimal conditions for proper image reconstruction.

2.5 Ptychographic Imaging

So far, we have discussed the technical aspects of our ptychography microscope, including its essential hardware and software parts. In this section, we will demonstrate the ability of our ptychographic microscope to acquire and reconstruct both amplitude and phase images. To this end, we imaged various samples, selecting representative examples of inorganic samples, such as polymer beads and tissues, as well as organic specimens, including human and plant cells.

2.5.1 Imaging of synthetic samples

Polystyrene beads

Polystyrene beads of different sizes, from 1 to 15 μm, were purchased from Bang Laboratories, Inc. A stock solution of beads was diluted 1:1000 in MilliQ-water, and then a calibrated volume (100 μL) of the resulting dilution was dropped onto a cover glass. After complete water evaporation, the beads were covered with a glass cover and sealed with nail polish. For the ptychographic experiments, the sample was scanned with a step size of 3 μm, and diffraction patterns were collected from 2048 positions. For each position, we recorded 2 frames with an exposure time of 10 ms. As shown in Figure 2.7A, we got a clear reconstruction of both phase and amplitude of polystyrene beads with size as small as 4 μm. As expected, the phase has a radial distribution, from the border to the center of the beads, that well agrees with the optical path of a spherical and optically homogenous object.
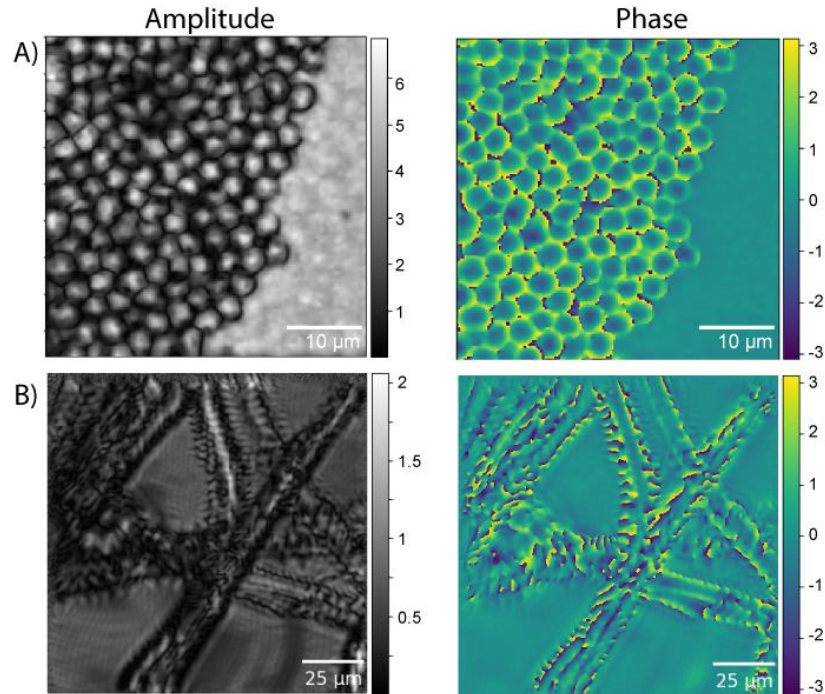
Figure 2.7. Reconstructed amplitude and phase images of (A) 4 μm polystyrene beads and (B) the fibers of a cleaning tissue.

Cleaning tissue

The second synthetic sample we tested is a lens cleaning tissue (Thorlabs, MC-5) consisting of organic fiber sheets. For the ptychography experiment, a small piece of tissue was cut, rinsed with a drop of MilliQ-water, and closed between two cover glasses. The diffraction patterns were collected from 2048 positions with a step size of 3 μm. For each position, we recorded 5 frames with an exposure time of 10 ms. From the reconstructions shown in Fig. 2.7B we can clearly see the fibrous structures of the sample.

2.5.2 Imaging of biological samples

Onion cells

Onion's epithelium is a sample easy to find and can provide cells with a regular shape and large size. As such, this sample is suitable for testing a large field of view imaging system as our

ptychography microscope. Considering that the average size of an onion cell is of the order of 50 μm ×150 μm, the scan was performed on 2048 points with a step size of 5 μm. This resulted in a FOV large enough to image an entire cell. Another problem with onion cells is the poor refractive index contrast of their constituents. Indeed, onion cells mainly consist of water, and only the presence of the cell membranes provide some degree of contrast. As a result, onion cells poorly scatter light and, hence, produce diffraction patterns with not sufficient intensity contrast for proper image reconstruction. However, the large parameter space of our ptychography microscope offers the possibility of mitigating this problem. For the imaging, we offset the Z_{43} at 200-250 μm and Z_{24} at 0, while keeping the cells at the focal plane of the illumination objective. As shown in Figure 2.8 the strategy was successful, indeed a clear image of both the amplitude and phase of the onion cell was properly reconstructed. In particular, we were able to recognize specific structures of the cells, such as the cell wall and the nucleus.
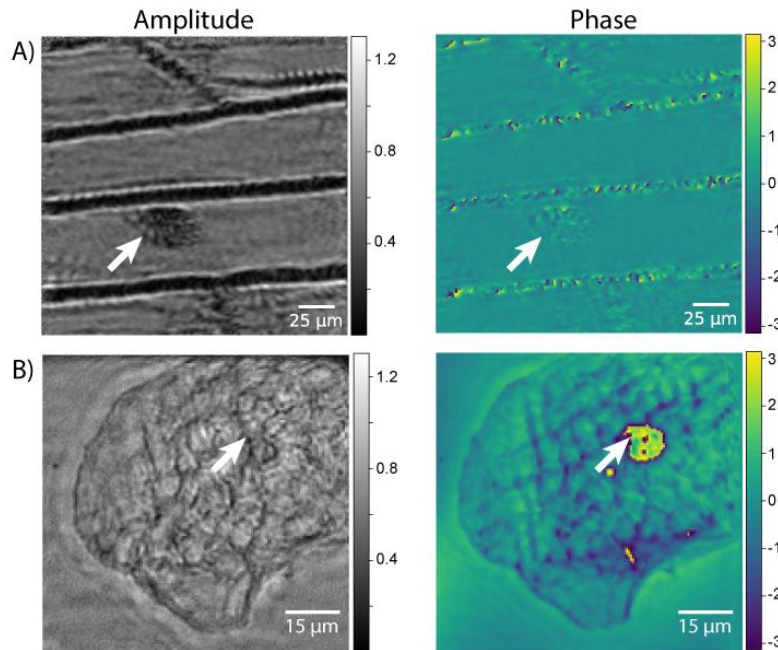
Figure 2.8. Reconstructed amplitude and phase of (A) onion cells and (B) a cheek cell. The regular shape of the onion cells, delimited by the cell wall, and the nucleus of a single cell are clearly visible in both amplitude and phase (white arrows). Notably, in (B) the phase reconstructing capability of our technique provides a clear identification of the nucleus of a cheek cell (white arrows), whose signal is barely visible in the amplitude map.

Cheek cells

As representative examples of biological samples we can study with our ptychography microscope, we selected cheek cells. We focused on these cells because they are easy to prepare and collect. Moreover, from a biological viewpoint, cheek cells are widely used for performing cost-effective, painless, and minimally invasive DNA extraction procedures[10]. However, imaging cheek cells with ptychography poses additional challenges with respect to onion cells because they not only weakly scatter light but also possess a more complex cellular organization. In spite of the increased difficulties, we were able to collect high-quality amplitude and phase images of cheek cells (Figure 2.8B). The diffraction patterns were collected from 2048 positions with a step size of 2 μm. For each position, we recorded 2 frames with an exposure time of 10 ms. We offset the Z_{43} at 200 μm and Z_{24} at 5 μm. Notably, we can clearly distinguish the nucleus in the retrieved phase image and, hence, its different reactive index or protein content with respect to the rest of the cell body. This suggests that ptychography has the potential to image the refractive index of target samples, a feature of great interest for research and industrial applications as important as biology or polymer science.

2.6 Microscope characterization

The previous results indicate the potentialities of our microscope as a tool for either biological studies or material characterizations. The open question is determining the performance of the system. To answer this question, we performed a systematic experimental study aimed at finding the figure of merit of the ptychographic microscope in terms of field of view, spatial resolution, and image contrast. The results of this study are presented next.

USAF resolution target

Initially, we tested the microscope with a resolution target (Thorlabs, R3L3S1N), namely, an amplitude mask with a dark background and transparent features. As shown in Figure 2.9A, the target has 10 groups, labeled with progressive numbers from -2 to +7, with six elements each. The maximum resolution of the target is 228-line pairs per millimeter. As such, this sample offers the possibility of systematically studying the resolution of our microscope. In particular,

we restricted the acquisitions to the two smallest groups (labeled as +6 and +7 in Figure 2.9A). To collect the diffraction patterns generated by illuminating the USAF sample, we performed several scans of 1024 points with a step size of 3 µm. The sample was placed 200 µm below the virtual detector plane and 5 µm above the focus of the illumination objective. This configuration produced a field of view of 90 µm as expected (see equations 2.2).

By using this setting, we were able to image all the elements of the 6th group (not shown) and the first 5 elements of the 7th group. Notably, the features of the amplitude image well adhere to that of the target, though the phase map shows a surprising degree of phase delay between the blocked and transmitted waves. We believe that this artifact might be due to geometrical aberrations (spherical aberrations) introduced by the thickness of 1.5 mm of the target. This hypothesis also explains why we weren't able to image the smallest element of the 7th group and the apparent measured resolution of only 8.87 and 9.42 µm for the amplitude and phase images, respectively (Figure 2.9C, D). As detailed next, to erase any doubts about the real resolution of our microscope, we decided to perform additional tests with an ad-hoc sample.

Phase grating

To mitigate the risk of introducing geometrical aberrations, we prepared a phase grating onto a glass coverslip whose thickness (150 µm) is selected to minimize spherical aberrations of microscopy objectives. We used a femtosecond laser to ablate periodic lines into the topmost surface of the coverslip. Readers can find details about our laser ablation workstation in the published literature[11]. We collected diffraction patterns and reconstructed images of the phase grating with the same hardware and software parameters employed for the resolution target.

Figure 2.10A shows the reconstructed amplitude and phase images of a grating with a periodicity of 15 µm and reconstructed using 500 iterations. Interestingly, the amplitude image not only resolves the periodicity of the grating but also fine details of the ablated trenches, such as their lateral roughness. In particular, from this image, we inferred the spatial resolution by using decorrelation analysis. A detailed description of this method goes beyond the scope of this thesis, and readers interested in a deeper understanding of the technique can refer to recent literature[12]. Briefly, the idea is to find the resolution by studying the cross-correlation between a low-pass-filtered and a high-pass filtered version of the original image for closer and closer cut-off frequency of the two filters. The resolution R is determined when the filtered images stop
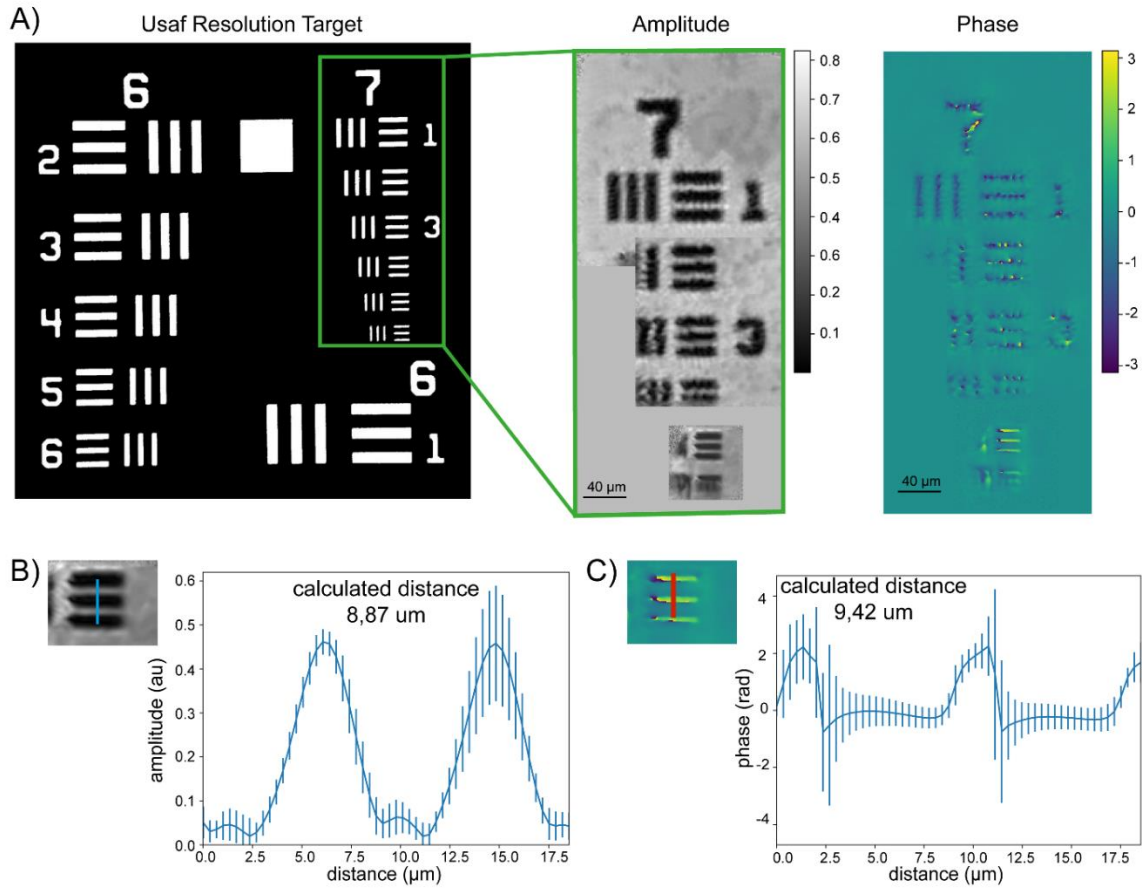
Figure 2.9. A) Picture of the USAF resolution target and reconstructed both amplitude and phase images of the elements in the 7th group. B, C) Measured average and error bars (3 standard deviations (STD)) of the amplitude and phase profiles of the 5th element of the group.

correlating and it is calculated as $R = 2\, d_I / r_{max}$ where d_I is the image pixel size and r_{max} is the maximum radius of the filtering mask (Figure 2.10B). We applied this decorrelation analysis to the amplitude images reconstructed for various number of iterations, and we obtained a resolution R=2.02±0.26 µm (Figure 2.10C). This result reveals the real potential of our ptychography microscope whose spatial resolution for thin samples goes beyond the 9 µm we observed with the USAF target. Following this positive result, we further stressed the system successfully by imaging clusters of beads with size of only 1 µm (Figure 2.11).
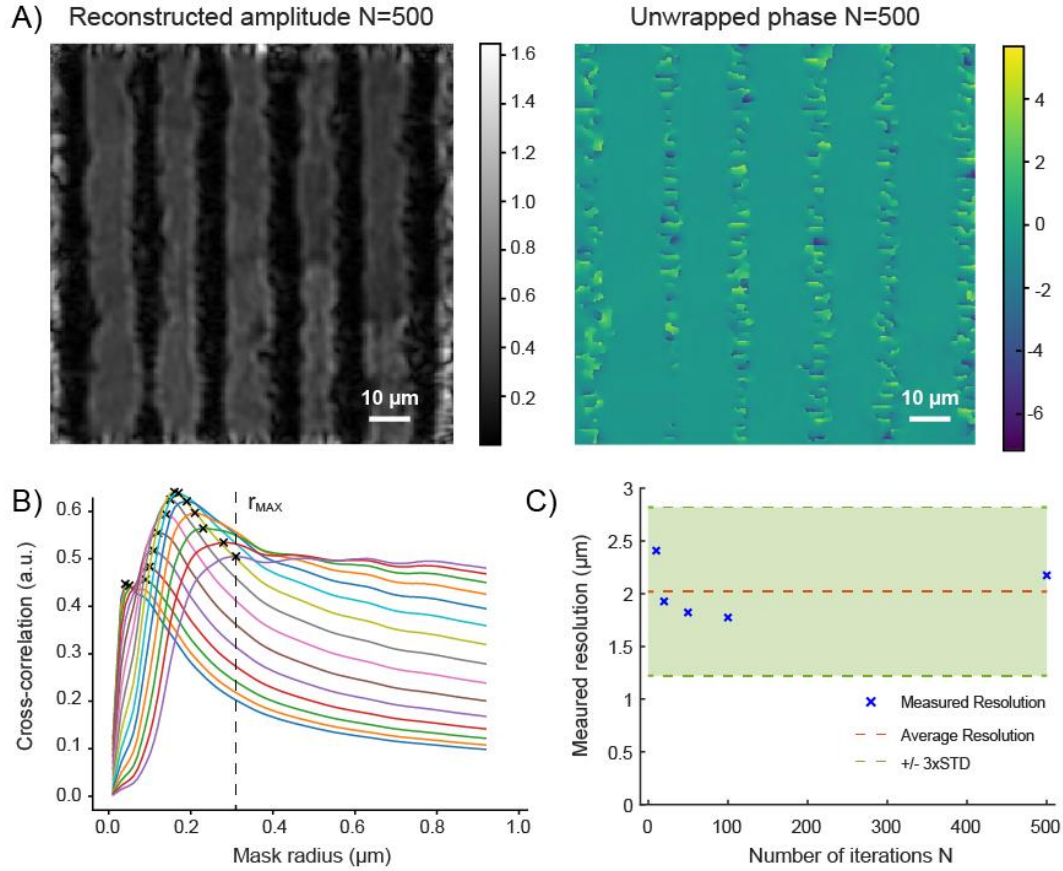
Figure 2.10. A) Reconstructed amplitude and phase of the laser-ablated grating; B) Representative examples of the cross-correlation curves used for computing the image resolution. C) Measured spatial resolution (blue symbols) for various numbers of reconstruction iterations. The dashed red line denotes the average resolution, while the green dashed lines the resolution upper and lower limits.

It should be noticed that the measured resolution ($R \sim 1$ µm) is still larger than the theoretical limit and, hence, we believe that further optimizations of the setup are possible. Regarding the phase image of the laser-ablated grating, we easily recognized the flat glass regions, whereas the phase values of the trenches exhibited too much dispersion to perform a quantitative analysis. We supposed that this might be due to the irregular bottom-surface of the ablated trenches. For this reason, we planned to perform a study on the sensitivity of the microscope to optical path variations. Results of this investigation are presented in the next chapter.
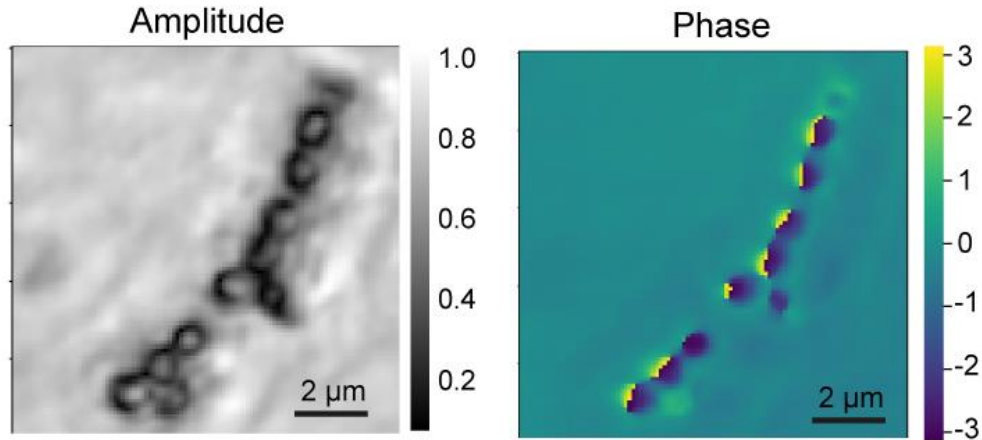
Figure 2.11. Reconstructed amplitude and phase of polystyrene beads with a size of 1 µm.

Finally, we used the same grating sample to study the contrast of the reconstructed images for various reconstruction iterations (N). Figure 2.12 summarizes the results of this study. In particular, for $N<10$, the reconstruction algorithm failed, returning a noisy image. For $N>10$, on the other hand, the reconstruction worked properly, and, more importantly, the contrast of the amplitude images reached a value close to the ideal contrast of 1 for $N \sim 20$. Therefore, considering the substantial independence of the spatial resolution from the number of iterations, we selected N between 20 and 100 for the remaining part of this thesis. Notably, we didn't study the contrast of the phase image because 1) for the wrapped phase clearly it is 2π and 2) the high dispersion of the phase of the ablated trenches impedes a precise quantitative analysis even after phase unwrapping.

To conclude this chapter, we designed and implemented a ptychographic optical microscope. We proved that the system is not only functional but also determined the range of feasible field of view (up to 170 µm wide), contrast (close to ideal unity), and resolution (1 µm). Although there are chances for improvements, the overall figure of merit of our microscope suggests it might be applied to the study of biological questions, a possibility we explored in Chapter 4.
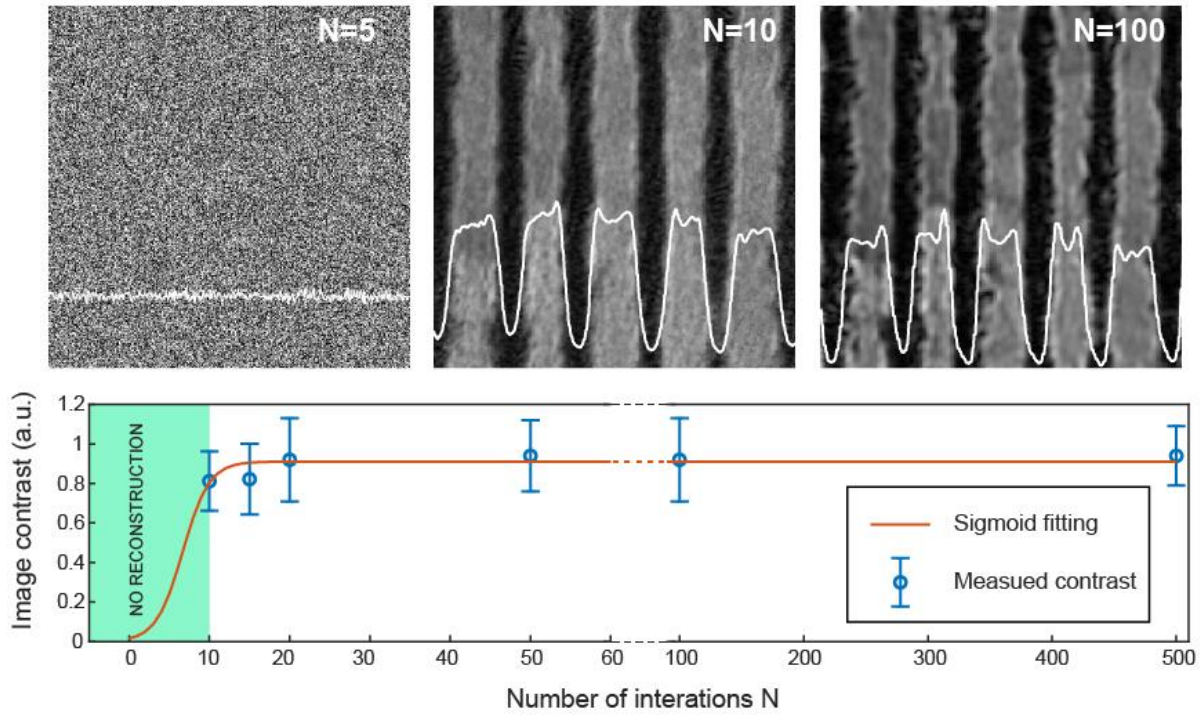
Figure 2.12. Experimental study of the image contrast vs. the number of iterations. Examples (top) of output images obtained for a number of iterations N=5, 10, and 100. The reconstruction process requires a minimum number of iterations that we found to be 10. The image contrast rapidly rises, reaching a plateau corresponding to a near-unity contrast.

Bibliography

1.   Anthony, N. *et al.* Ptychographic imaging of NaD1 induced yeast cell death. *Biomed. Opt. Express* **10**, 4964 (2019).

2.   Huang, X. *et al.* Optimization of overlap uniformness for ptychography. *Opt. Express* **22**, 12634–12644 (2014).

3.   Virtanen, P. *et al.* SciPy 1.0: fundamental algorithms for scientific computing in Python. *Nat. Methods* **17**, 261–272 (2020).

4.   Edelstein, A. D. *et al.* Advanced methods of microscope control using μManager software. *J. Biol. Methods* **1**, e10 (2014).

5.   Rodenburg, J. & Maiden, A. *Ptychography*. (2019).

6.   Vogel, H. A better way to construct the sunflower head. *Math. Biosci.* **44**, 179–189 (1979).

7.   Collette, A. *Python and HDF5*. (O'Reilly, 2013).

8.   Maiden, A. M. & Rodenburg, J. M. An improved ptychographical phase retrieval algorithm for diffractive imaging. *Ultramicroscopy* **109**, 1256–1262 (2009).

9.   Rodenburg, J. M. & Faulkner, H. M. L. A phase retrieval algorithm for shifting illumination. *Appl. Phys. Lett.* **85**, 4795–4797 (2004).

10.   Küchler, E. C. *et al.* Buccal cells DNA extraction to obtain high quality human genomic DNA suitable for polymorphism genotyping by PCR-RFLP and Real-Time PCR. *J. Appl. Oral Sci.* **20**, 467–471 (2012).

11.   Surdo, S., Piazza, S., Ceseracciu, L., Diaspro, A. & Duocastella, M. Applied Surface Science Towards nanopatterning by femtosecond laser ablation of pre-stretched elastomers. **374**, 151–156 (2016).

12.   Descloux, A. & Radenovic, A. Parameter-free image resolution estimation based on decorrelation analysis. **16**, (2019).

3 Refractive index imaging

3.1 Introduction

As anticipated in Chapter 1, the refractive index (RI) is an optical property of a material playing a key role in the phenomena of light-matter interactions. Measuring a materials RI is fundamental in many research and industrial fields[1]. In particular, the RI provides information about the specimen under observation not only in terms of the material optical behavior, but it can also be used to monitor industrial and biological processes providing (bio)chemical identification and concentration of species as well as density, purity, and even temperature of the sample[2]. For biomedical applications, refractive index measurements are relevant for diagnostic and therapeutic purposes and, more in general, for conducting biological research[3], both *in vivo* and *in vitro*. For instance, RI measurements have been used in cellular biology for blood characterization[4], to study cell cytoplasm[5] and even their mutations in cancer[6]. In fact, since tumor cells show alterations in the refractive index of the cytoplasm, the latter can be used as an optical indicator of tumor cells.

Nowadays, there are plenty of techniques for measuring the RI of a specimen. Among others, refractometry is probably the most widely used approach. In general, a refractometer transduces a variation of refractive index into a change of an optical parameter such as the reflection angle, as in the Abbe refractometer[7], the spectral shift of a resonance mode as in photonic micro- and nano-cavities[8-9-10], or the phase delay of light waves as in interferometry[11-12]. Regardless of the specific implementation, the figure of merit of any refractometer is given by its linear range (LR), sensitivity (S), and limit of detection (LoD)[13]. The linear range is the span of the calibration curve, namely the RI sample vs. measured optical parameter, which displays a linear relationship. The sensitivity is the slope of the calibration curve; depending on the parameter selected for the measurement, it can be expressed in angle per refractive index unit

(°/RIU or rad/RIU, where RIU is a standard measure unit of the RI refractometry) or length per refractive index unit (nm/RIU). The limit of detection is the smallest refractive index variation that can be measured. So far, state of the art refractometry is capable of detecting RI values within linear ranges as large as 0.3 RIU[14], and at a sensitivity (for bulk RI) as high as 5.9×10^4 nm/RIU and 1864 π/RIU and limit of detection as small as 5×10^{-8} RIU[15-16]. Considering the impressive performance of refractometry is not surprising that its applications have expanded from chemical to biochemical analysis[17] and cellular biology[18]. As a matter of fact, the refractive index has evolved from a pure optical parameter to a biological indicator for studies of 1) biological samples, such as *in vitro* or *in vivo* cells, and 2) drug formulations, proteomics, and even environments[19]. For instance, an Abbe refractometer was successfully used to study the hemoglobin[4,20] concentration of red blood cells, using the RI as a marker of diabetes[4]. Nevertheless, traditional refractometric approaches only provide an effective refractive index, meaning a RI averaged over the volume where light-matter interactions occur. As such, the spatial distribution of the refractive index and thus relevant information about the composition of the specimen are lost. A possible solution to this problem is scanning the specimen with the probing light[12-21-22] or multiplexing the refractometer devices[23]. However, these approaches can be costly because they are time consuming, compatible with thin samples only, and require ad-hoc functionalization protocols.

A method to address the above problems is using optical microscopy to image the refractive index of a sample. Indeed, since the outcome of any microscope is an image, this strategy intrinsically provides spatially resolved information[24]. Furthermore, optical microscopy is the tool of choice for biological studies, which is the target application of this thesis. Among the possible microscopy techniques, we are interested in those that allow reconstructing the phase of light after interacting with the sample. The phase delay Δφ is related to the refractive index of the sample and its thickness by the optical path difference (OPD)[25]:

$$\Delta\varphi = \frac{2\pi}{\lambda} OPD = \frac{2\pi}{\lambda} \int n(s)\, ds \qquad (3.1)$$

where $n(s)$ is the sample refractive index along the light propagation direction (the s coordinate), and λ is the wavelength of light. Knowing λ, we can therefore obtain the OPD map
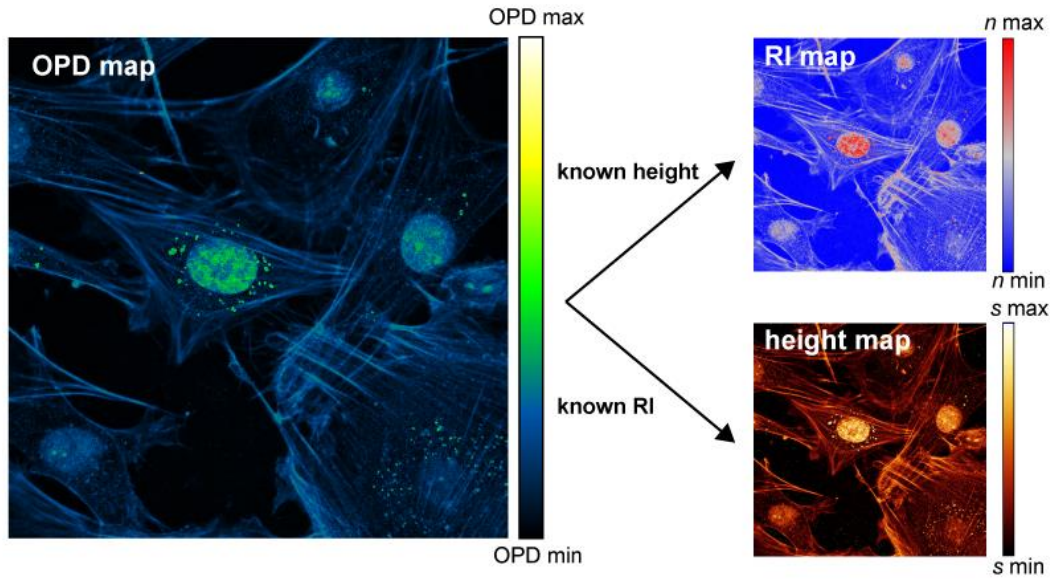
Figure 3.1. Concept of information retrieval from a phase map. A) OPD distribution and B) RI map (top) and height map (bottom) extracted from A under the assumption of constant height and constant RI sample, respectively.

and retrieve the RI distribution of the sample if we know its morphology[22] and vice versa (Figure 3.1).

The microscopy family used for imaging $\Delta\varphi$ or OPD includes differential interference contrast (DIC) and quantitative phase imaging (QPI) techniques. DIC indirectly measures the phase shift as the intensity of light resulting from the interference between waves traveling through the sample and a reference wave. As such, the OPD distribution due to the thickness and RI of the sample is transduced into a greyscale image; the pixels value ranges from 0 for destructive interference to 1 for constructive interference. The problem with DIC is that it is a semi-quantitative technique because the amplitude of the recorded light can also be altered by absorption, reflection, or scattering. To have a more precise and reliable measure of the OPD, it is, therefore, necessary to directly measure the phase delay introduced by the sample and record it as pixel values. This is the case for QPI techniques that exploit interferometry approaches to measure the delay between a beam transiting through the sample and a reference. Examples of QPI methods include optical coherent tomography[26], holography[27], and ptychography[28]. In the context of biology, tomography has been successfully used to recover nuclear and whole-cell 3D

rendering of the RI, with a subcellular resolution of both fixed[29] and flowing cells[30]. Interestingly, the RI of the nucleus was found lower than that of cytoplasm in different cell lines (e.g., for breast cancer cells MCF7, the $RI_{nucleus} = 1.3509 \pm 0.0042$, while $RI_{cytoplasm} = 1.3775 \pm 0.0058$). Also different values were found between cancerous and non-cancerous cells, indicating that RI can be used as possible indicator of cell unhealthiness[29].

Nevertheless, QPI approaches have some limitations. The microscope apparatus requires a precise alignment between the probing and reference beams, and it is sensitive to vibrations and external disturbances. For these reasons, in the thesis, we selected ptychography as a tool for imaging the RI of biological samples. Ptychography represents a cheaper and simpler solution with respect to the other QPI architectures. As we anticipated in Chapter 3, the technique can be implemented on commercial microscopes with minor efforts and benefits from a large number of open source resources available for data collection and image reconstruction. In Chapter 2, we have shown the potential of our ptychographic microscope in reconstructing the amplitude and phase of different samples. In this chapter, we will expand on the ability of our microscope to quantitatively measure the OPD and recover a RI map. We also provide an exhaustive characterization of the RI ptychographic microscope in terms of sensitivity, limit of detection, and range of linearity.

3.2 Experimental section

In this section, we describe and characterize the sample models we used to prove the ability of ptychography in imaging the refractive index. In particular, we focused our attention on two samples: 1) polystyrene beads and 2) polymeric microdisks.

Polystyrene beads. We initially tested the microscope with polystyrene beads because they are commercially available at high optical and chemical grades. As such, they provide precise and reliable refractive index values and size distribution. In particular, we selected polystyrene beads (Bang Laboratories, Inc) with a diameter of 15.45 ± 1.1 μm, with a RI of 1.587 ± 0.05, corresponding to a coefficient of variation CV<5%. For microscopy experiments, we diluted a
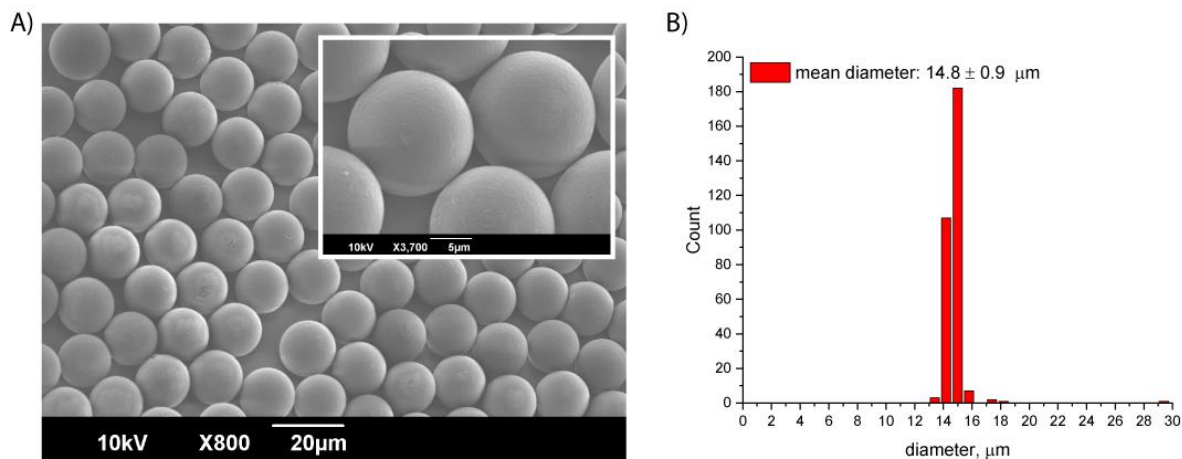
Figure 3.2. A) SEM image of the monolayer polystyrene beads used as calibrated RI reference. B) Measured size distribution confirming the supplier specification.

stock solution of beads in milli-Q water (1:1000), released 100 µL of the solution onto a #1.5 glass coverslip, and waited for complete evaporation of the water. This procedure resulted in clusters of monolayer beads as confirmed by scanning electron microscopy (SEM) measurements (Figure 3.2A). For ptychography experiments, the beads were covered with a glass coverslip and sealed using nail polish. Diffraction patterns caused by the beads were collected by placing the illumination plane 5 µm below the sample plane (i.e., Z_{24}= 5µm). The number of scanning positions (N=2048) and stepsize (1 µm) were chosen in order to obtain a FOV of 45 µm, to allow imaging of multiple beads (~ 9 beads) simultaneously. For each position, we acquired 5 images of the diffraction patterns, each with 10 ms of exposure time. Finally, we selected a distance between the sample and the virtual detector plane (Z_{43}= 70 µm) to push the pixel size down to 116 nm in order to better resolve the reconstructed phase maps.

<u>Polymeric microdisks</u>. To quantify the performance of the microscope as a refractive index imaging system, we selected polymeric microdisks with the shape of truncated cones. The lateral surface of the cone offers a linear distribution of known optical path lengths, suitable for experimentally building a calibration curve, namely the reconstructed phase vs. the optical path length. For this study, we fabricated the microdisks in our lab by using a laser additive manufacturing method. Readers interested in details of the technique can refer to the following papers[31,32]. In particular, we prepared arrays of microdisks made of a positive photoresist (S1913, Microhem Inc.) and deposited them on a polydimethylsiloxane (PDMS) substrate. The nominal
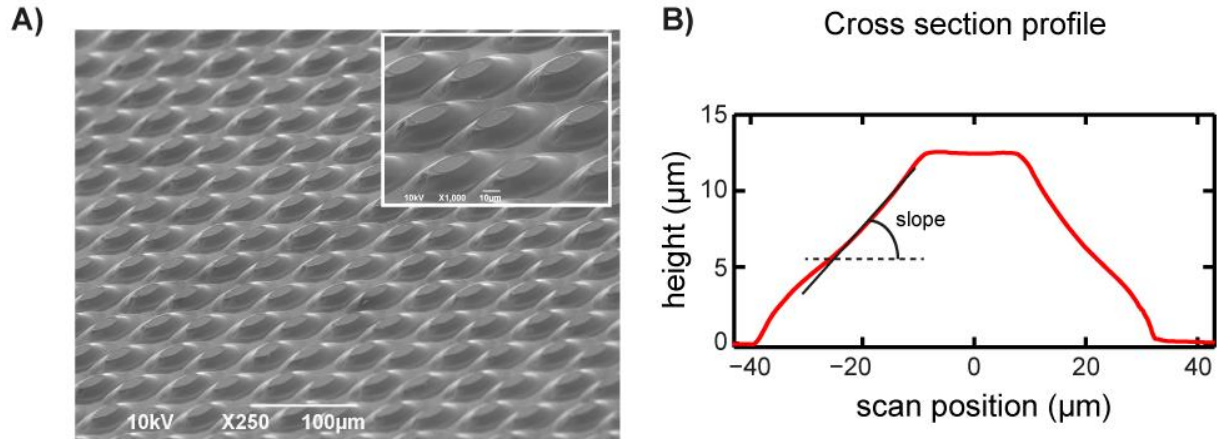
Figure 3.3. A) SEM image of the microdisks array. B) Representative cross-section height profile of a microdisk of (A). The slope of the lateral surface is ~0.4.

RI of the photoresist at the operational wavelength of our microscope (λ=561 nm) is 1.62 RIU, though, we cannot exclude some alterations due to aging or excessive light exposure. In Figure 3.3A, it is possible to see a SEM image of the microdisks along with an enlarged detail of a few microdisks used to recover their height profile through an optical profilometer (Figure 3.3B). The analysis returned a height of the cone of approximately 12 μm and diameters of ~70 and 18 μm for the bottom and bases, respectively. From the SEM images, we can appreciate the quality of the lateral surface, although a systematic defect is present in each microdisk due to the manufacturing process. For imaging the microdisks with ptychography, we recorded diffraction patterns by placing the illumination plane 1 μm below the sample plane (i.e., Z_{24} =1 μm) and scanning its surface over N=2048 positions with a step size of 1 μm. For each position, we recorded 2 images with 10 ms of exposure time each. Selecting a field of view FOV of 43 μm, we focused our attention on a single microdisk.

3.3 Results and discussion

Once the data were successfully collected, we reconstructed both the amplitude and phase for the model samples. Finally, we analyzed the phase images, which contain the information

about the optical path due to light passing through the sample, with the aim to characterize the sensing performance of our microscope.

Polystyrene beads. Figure 3.4A shows the reconstructed amplitude and phase images of a cluster of beads. Up to 7 beads are clearly distinguishable in agreement with the selected field of view. Note that the phase is wrapped, meaning that it presents abrupt discontinuities due to the boundaries we imposed to find a unique solution of the phase problem; i.e., to this end, the phase is constrained between $[-\pi,\pi]$. These constraints result in a "fake" phase map. To solve this problem, we unwrapped the phase, so we solved the phase discontinuities by summing 2π to pixels that differ from their neighbors more than 2π.
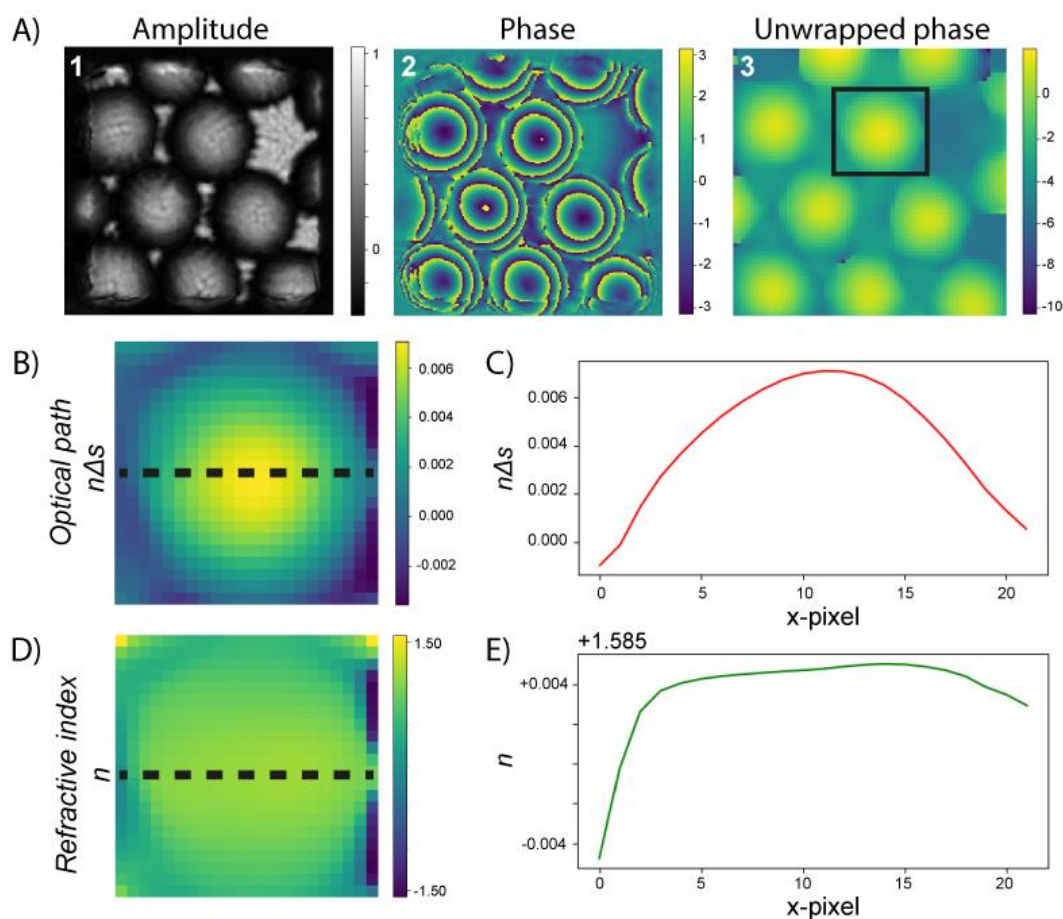

Figure 3.4. Refractive index retrieval with ptychography. A) Reconstructed (1) amplitude, (2) phase, and (3) the unwrapped phase of 15 µm polystyrene beads. B) Map and C) Cross-section profile of the optical path difference OPD of a single bead. D) Retrieved refractive index distribution and E) cross-section profile of a polystyrene bead. For this experiment, the pixel size is 116 nm.

To recover the refractive index of polystyrene, we focused our attention on the unwrapped phase of a single bead. In particular, knowing the operational wavelength of our microscope, we derived the OPD distribution of the bead (Figure 3.4B). Notably, the OPD well resembles the shape of a spherical bead with a homogeneous refractive index. This is further corroborated by the cross-section profile of the OPD (Figure 3.4C). If we approximate the bead as a sphere with radius R = 7.5 μm and the center located in the origin of XY coordinate system, we can calculate the OPD by integrating equation 3.1 over the entire hemisphere as follows:

$$OPD(x,y) = n\Delta s(x,y) = n\sqrt{R^2 - x^2 - y^2} \tag{3.2}$$

From equation 3.2, we can now calculate the RI as:

$$n = \frac{OPD(x,y)}{\sqrt{R^2 - x^2 - y^2}} \tag{3.3}$$

Figure 3.4D, E shows the refractive index map and its cross-section profile, which clearly indicates a constant RI value as expected for this sample. Precisely, we found RI=1.585 ± 0.004, which is close to the value provided by the supplier (1.587 ± 0.05).

So far, we have ascertained that ptychography is capable of retrieving the RI of a calibrated sample. The open question is determining the sensing performance of our system. As detailed next, to shed light on this point, we performed additional experiments on the microdisks.

Microdisks array. Figure 3.5 shows a representative example of the reconstructed amplitude and phase of a portion of the microdisks array. Although the amplitude image appears slightly blurry, the top and lateral surfaces of the disk are clearly visible. The phase map well agrees with the amplitude image, although the phase profile along the lateral sidewalls of the disk is wrapped between [–π,π]. To compute the sensing performance, it was, therefore, necessary to unwrap the reconstructed phase. The result of this operation is shown in Figure 3.6A. It should be noted that the unwrapped phase still exhibits some degree of "roughness", which can be due to either the reconstruction process or artifacts created by the unwrapping procedure. To mitigate this problem, we filtered out high frequency components of the unwrapped phase with a Wiener filter (Figure 3.6B). The resulting image was used to extract the calibration curves of the RI imaging
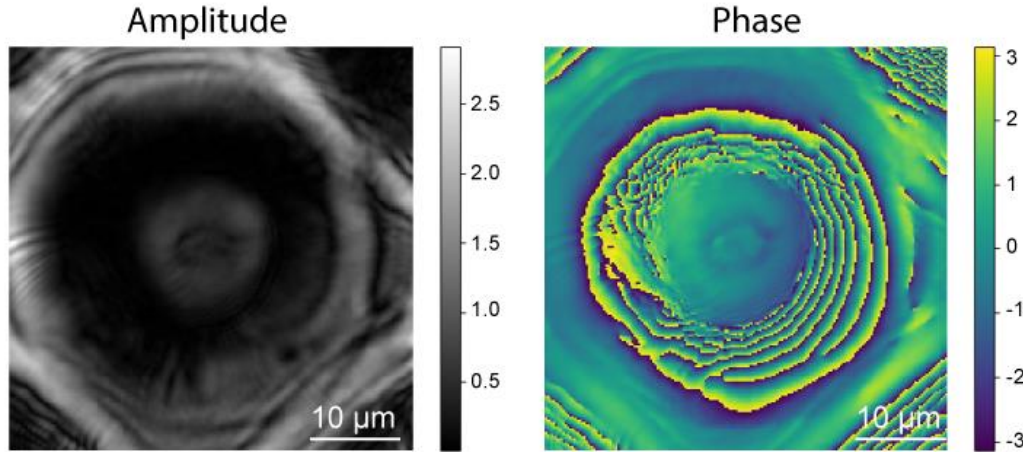
Figure 3.5. Reconstructed amplitude (left) and phase (right) images of a single polymeric microdisk.

system, namely, the measured phase delay (red lines in Figure 3.6B) vs. the optical path difference experienced by light waves traveling through the lateral and tilted surface of the disk. As detailed next, the resulting calibration curve (Figure 3.6C) was finally used to quantify the sensing performance of our system.

The figure of merit of the ptychography microscope as a refractive index imaging system was determined by taking into account several analytical parameters, namely sensitivity (S), limit of detection (LoD), range of linearity (L), coefficient of variation (CV). Sensitivity values, by definition the measured phase shift versus optical path difference $S = \delta\varphi/\delta OPD$, are calculated as the slope of the linear-regression best fitting calibration curve data. The limit of detection LoD is the ratio between the resolution R and the sensitivity S, and it is calculated by taking R equal to 3 standard deviations (STD) of the phase shift of the reference OPD. Range of linearity L is evaluated as the range of optical path difference within which the calibration curve is linear, and it is evaluated in terms of the squared correlation R^2 coefficient of the linear regression curve best fitting the experimental data. The CV coefficient is evaluated as $\%CV = \sigma_\varphi/\mu_\varphi \times 100$ with σ_φ standard deviation and μ_φ mean value of the experimental phase.

In this study, we observed a linear relation ($R^2 > 0.99$) over the entire range of exploited OPD and measured a sensitivity $S=5.34\times10^6$ rad/m·RIU with a detection limit LoD= 8.8×10^{-7} m·RIU. To better understand the sensing performance of the system we split the sensitivity into
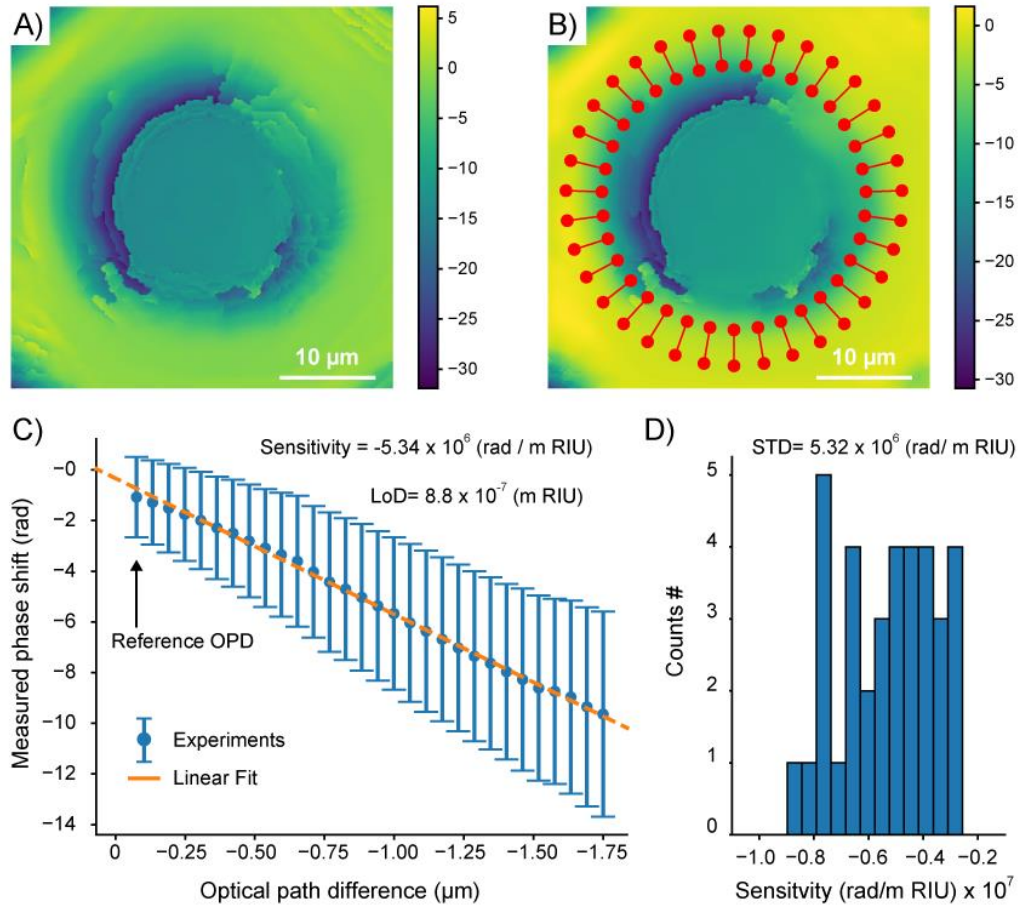
Figure 3.6. **Sensing performance of the ptychography RI imaging system.** A) Unwrapped phase map of a microdisk imaged with ptychography. B) Phase map subjected to low-pass filtering procedure. The red lines denote the phase profiles used to build the calibration curve of the system. C) Measured phase shift, mean values (symbol) and 3 standard deviations (error bars), vs. optical path difference introduced by the lateral surface of the microdisk. The orange line is the linear regression curve best fitting the experimental data. D) Distribution of the sensitivity over the extracted calibration curves.

thickness sensitivity (for constant RI) and refractive index sensitivity (for constant sample thickness t_S). Considering a sample with a constant RI=1.35, which is representative of biological matter, we calculate that our system is able to detect thickness variations Δt_S with a sensitivity S~7.2×10^6 rad/m and a limit of detection LoD~650 nm. Therefore, our system can resolve sub-micrometric features of the sample along the direction of light propagation. On the other hand, if we consider a sample with an even thickness, the RI sensing performance will be:

1) sensitivity S ranging from 5.34 mrad/ RIU to 534 rad/RIU and 2) LoD from 8.8 to 0.088 RIU for t_S between 1 nm and 10 µm. Clearly, an LoD=8.8 RIU has no physical meaning, especially with visible wavelengths and biological samples. Therefore, for biological samples with a thickness below 10 nm we cannot resolve almost any reasonable refractive index variation. This figure of merit suggests that as RI imaging system, our microscope is suitable for large samples such as cells and with a modest detection limit. However, it should be noted that the sensitivity of the system has a wide dispersion (Figure 3.6D), and, theoretically, the S values can double its average leading to improved sensing performance. We believe that this large dispersion and consequent degradation of the sensing performance is due to the limited reliability of the measured phase over the entire disk surface; this hypothesis is in agreement with the large coefficient of variation (CV~40%) we obtained for this study. This variability could be ascribed to the presence of systematic defects on the microdisk surface, which are due to the fabrication process, as visible from the SEM images (Figure 3.3A).

Therefore, to achieve a more precise quantification of the RI sensing performance, we restricted the analysis to a quarter of the microdisk. Figure 3.7A shows the calibration curve resulting from this more focused analysis, which led to a CV of 9.9% and, thus, a more reliable

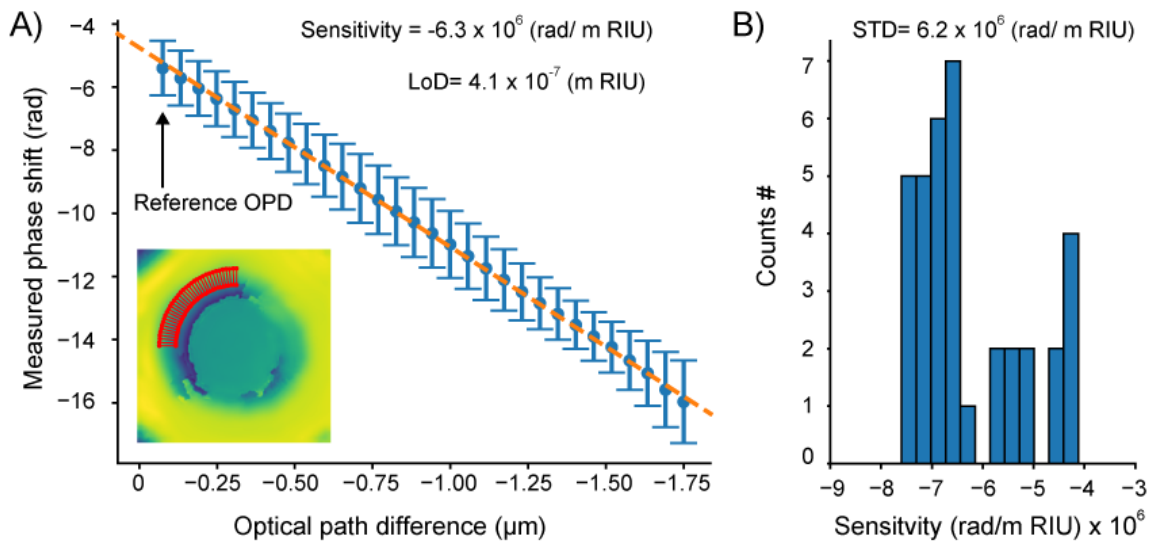**Figure 3.7.** A) Measured phase shift, mean values (symbol) and 3 standard deviations (error bars), vs. optical path difference introduced by the lateral surface of the disk. The inset shows the quarter of the phase map used for this study. The orange line is the linear regression curve best fitting the experimental data. B) Distribution of the sensitivity over the extracted calibration curves.

measurement. For this study, we measured sensitivity $S=6.3\times10^6$ rad /m·RIU and a detection limit LoD$=4.1\times10^{-7}$ m·RIU. Simply put, the sensitivity slightly improved, but the detection limit reached half the initial value. In other words, the system is now capable of resolving the thickness of a homogenous sample with a detection limit LoD~300 nm and the refractive index of an even 10-µm-thick sample with a LoD~0.04 RIU, this latter is sufficient to answer biological questions such as discriminating between healthy and unhealthy cells[33].

3.4 Conclusions

The ptychography microscope can effectively provide spatially resolved information about the phase and, therefore, the optical thickness of a sample. We found that the sensing performances of our system are comparable or superior to other phase imaging techniques. Indeed, the system is sensitive to optical path differences within a large linear range and with high reliability (CV~10%), sensitivity as high as $S=5.34\times10^6$ rad/m·RIU, and detection limit down to LoD$= 8.8\times10^{-7}$ m·RIU. In particular, for a homogenous sample (RI constant), the system resolved thickness variations as small as 300 nm, meaning that our ptychography microscope has axial resolution comparable with state-of-art methods such as confocal, two-photon, or light-sheet microscopes. On the other hand, as a refractive index imaging system, the microscope is suitable for analyzing the biochemical composition of thick samples (10 µm or higher) yet compatible with 2D ptychographic image reconstruction, but with detection limits small enough to answer relevant biological questions, such as cancer cells recognition.

Considering the results of this study, we believe that the integration of our ptychography system into a microscope capable of providing information about the thickness of the sample, such as atomic force[34], confocal, or light-sheet microscopes[35-36], will result in a multimodal imaging system with label-free cellular analysis operations. As detailed in the next chapter, we performed an explorative study regarding this option.

Bibliography

1.   Singh, S. Refractive Index Measurement and its Applications. *Phys. Scr.* **65**, 167–180 (2002).

2.   Willard, H. H., Merritt L L, J., Dean, J. A. & Settle F A, J. *Instrumental methods of analysis, 7th edition*. (Florence, KY (US); Wadsworth Publishing Company, 1988).

3.   Müller, P., Schürmann, M., Girardo, S., Cojoc, G. & Guck, J. Accurate evaluation of size and refractive index for spherical objects in quantitative phase imaging. *Opt. Express* **26**, 10729 (2018).

4.   Mazarevica, G., Freivalds, T. & Jurka, A. Properties of erythrocyte light refraction in diabetic patients. *J. Biomed. Opt.* **7**, 244–247 (2002).

5.   Steelman, Z. A., Eldridge, W. J., Weintraub, J. B. & Wax, A. Is the nuclear refractive index lower than cytoplasm? Validation of phase measurements and implications for light scattering technologies. *J. Biophotonics* **10**, 1714–1722 (2017).

6.   Backman, V. *et al.* Detection of preinvasive cancer cells. *Nature* **406**, 35–36 (2000).

7.   Paselk, R. A. The Evolution of the Abbe Refractometer. *Bull. Sci. Instrum. Soc.* **62**, 19–22 (1999).

8.   Surdo, S., Carpignano, F., Merlo, S. & Barillaro, G. Near-Infrared Silicon Photonic Crystals with High-Order Photonic Bandgaps for High-Sensitivity Chemical Analysis of Water-Ethanol Mixtures. *ACS Sensors* **3**, 2223–2231 (2018).

9.   Surdo, S., Carpignano, F., Strambini, L. M., Merlo, S. & Barillaro, G. Capillarity-driven (self-powered) one-dimensional photonic crystals for refractometry and (bio)sensing applications. *RSC Adv.* **4**, 51935–51941 (2014).

10.   Surdo, S. *et al.* Optofluidic microsystems with integrated vertical one-dimensional photonic crystals for chemical analysis. *Lab Chip* **12**, 4403–4415 (2012).

11.   Ahsani, V., Ahmed, F., Jun, M. B. G. & Bradley, C. Tapered fiber-optic mach-zehnder interferometer for ultra-high sensitivity measurement of refractive index. *Sensors*

(Switzerland) **19**, (2019).

12.   Bello, V., Simoni, A. & Merlo, S. Spectral Interferometric Detection of NIR Optical
       Resonances of Rectangular Microcapillaries for Refractive Index Sensing. *IEEE Trans.
       Instrum. Meas.* **70**, (2021).

13.   White, I. M. & Fan, X. On the performance quantification of resonant refractive index
       sensors. *Opt. Express* **16**, 1020–1028 (2008).

14.   Collier, C. M., Nichols, J. & Holzman, J. F. 4 - Digital microfluidics technologies for
       biomedical devices. in *Microfluidic Devices for Biomedical Applications* (eds. Li, X.
       (James) & Zhou, Y.) 139–164 (Woodhead Publishing, 2013).
       doi:https://doi.org/10.1533/9780857097040.1.139

15.   Liu, Q. *et al.* Highly sensitive Mach–Zehnder interferometer biosensor based on silicon
       nitride slot waveguide. *Sensors Actuators B Chem.* **188**, 681–688 (2013).

16.   Vala, M., Etheridge, S., Roach, J. A. & Homola, J. Long-range surface plasmons for
       sensitive detection of bacterial analytes. *Sensors Actuators B Chem.* **139**, 59–63 (2009).

17.   Tang, J., Qiu, G., Zhang, X. & Wang, J. A 3D-cascade-microlens optofluidic chip for
       refractometry with adjustable sensitivity. *Lab Chip* **21**, 3784–3792 (2021).

18.   Lue, N. *et al.* Live cell refractometry using hilbert phase microscopy. *Opt. InfoBase Conf.
       Pap.* 13327–13330 (2006). doi:10.1364/bio.2006.sh1

19.   Brolo, A. G. Plasmonics for future biosensors. *Nat. Photonics* **6**, 709–713 (2012).

20.   Liu, S., Deng, Z., Li, J., Wang, J. & Huang, N. Measurement of the refractive index of
       whole blood and its components for a continuous spectral region. *J. Biomed. Opt.* **24**, 1
       (2019).

21.   Barillaro, G., Merlo, S., Surdo, S., Strambini, L. M. & Carpignano, F. Optical quality-
       assessment of high-order one-dimensional silicon photonic crystals with a reflectivity
       notch at $\lambda \sim 1.55$ μm. *IEEE Photonics J.* **2**, 981–990 (2010).

22.   Merlo, S. *et al.* Label-free optical detection of cells grown in 3D silicon microstructures.
       Lab Chip **13**, 3284–3292 (2013).

23.   Cunningham, B. T., Zhang, M., Zhuo, Y., Kwon, L. & Race, C. Recent Advances in Biosensing with Photonic Crystal Surfaces: A Review. *IEEE Sens. J.* **16**, 3349–3366 (2016).

24.   Grubb, D. T. Optical Microscopy. *Polym. Sci. A Compr. Ref. 10 Vol. Set* **2**, 465–478 (2012).

25.   Bohannon, K. P., Holz, R. W. & Axelrod, D. Refractive Index Imaging of Cells with Variable-Angle Near-Total Internal Reflection (TIR) Microscopy. *Microsc. Microanal.* **23**, 978–988 (2017).

26.   Villone, M. M. *et al.* Full-angle tomographic phase microscopy of flowing quasi-spherical cells. *Lab Chip* **18**, 126–131 (2017).

27.   Balasubramani, V. *et al.* Roadmap on digital holography-based quantitative phase imaging. *J. Imaging* **7**, (2021).

28.   Kou, S. S., Waller, L., Barbastathis, G. & Sheppard, C. J. R. Transport-of-intensity approach to differential interference contrast (TI-DIC) microscopy for quantitative phase imaging. *Opt. Lett.* **35**, 447–449 (2010).

29.   Steelman, Z. A., Eldridge, W. J., Weintraub, J. B. & Wax, A. Is the nuclear refractive index lower than cytoplasm? Validation of phase measurements and implications for light scattering technologies. *J. Biophotonics* **10**, 1714–1722 (2017).

30.   Dardikman, G. *et al.* Integral refractive index imaging of flowing cell nuclei. *Opt. InfoBase Conf. Pap.* **Part F99-C**, 88–92 (2018).

31.   Surdo, S., Diaspro, A. & Duocastella, M. Geometry-controllable micro-optics with laser catapulting. *Opt. Mater. Express* **9**, 2892 (2019).

32.   Surdo, S., Carzino, R., Diaspro, A. & Duocastella, M. Single-Shot Laser Additive Manufacturing of High Fill-Factor Microlens Arrays. *Adv. Opt. Mater.* **6**, (2018).

33.   Jian, A. *et al.* Enhancement of the volume refractive index sensing by ROTE and its application on cancer and normal cells discrimination. *Sensors Actuators A Phys.* **313**, 112177 (2020).

34.   Canale, C., Jacono, M., Diaspro, A. & Dante, S. Force spectroscopy as a tool to investigate the properties of supported lipid membranes. *Microsc. Res. Tech.* **73**, 965–972 (2010).

35.   Piazza, S., Bianchini, P., Sheppard, C., Diaspro, A. & Duocastella, M. Enhanced volumetric imaging in 2-photon microscopy via acoustic lens beam shaping. *J. Biophotonics* **11**, 1–11 (2018).

36.   Duocastella, M. *et al.* Fast Inertia-Free Volumetric Light-Sheet Microscope. *ACS Photonics* **4**, 1797–1804 (2017).

4 Multimodal studies of genetic diseases:

The case of Progeria syndrome

4.1 Introduction

In the previous chapter, we have shown that our ptychographic microscope can spatially resolve optical path variations with high sensitivity and low detection limits, whatever they are due to thickness or refractive index variations. Among others, the study of chromatin organization in living cells is essential to answer relevant biological questions. Chromatin is a complex of DNA and proteins whose primary function is to package long DNA molecules into compact structures[1-2]. This is a delicate operation that, if wrongly performed, can result in severe morphological alterations and genetic tampering, which are responsible for diseases such as cancer. So far, the events that influence chromatin compaction in cells are still not clear. Being capable of imaging morphological alterations of cells, optical microscopy represents an ideal tool for shedding light on this point. Optical ptychography, in particular, can help study chromatin alterations by complementing morphology information (amplitude images) with spatially resolved refractive index measurements (phase images). Indeed, we hypothesize that different levels of chromatin compaction lead to different values of the average refractive index of the cell nucleus. To validate this, we selected the Hutchinson–Gilford progeria syndrome (HGPS) as a disease model caused by improper chromatin compaction. We believe that the deep investigation of this clinical case is of great interest, since it can lead to a better understanding of the mechanisms involved in chromatin compaction.

In order to effectively apply ptychography to the study of HGPS, we need to uniquely transduce the measurable optical path differences into refractive index maps. Simply put, we need information about the thickness distribution of the cells under observation. To this end, we combined ptychography with light-sheet and confocal microscopy; this is not the only option, and other techniques such as atomic force microscope would have worked as well. We selected confocal microscopy and light-sheet because they provide specificity, and the integration of ptychography into a standard, inverted confocal microscope is relatively straightforward.

We did not limit our possibilities to these two techniques. Indeed, we hypothesized that the polarization of light scattered by the sample, the same light used for ptychographic image reconstruction, could provide information about the chromatin organization[3]. Moreover, considering that chromatin organization also alters several intracellular pathways, we thought that a potential target could be cell-to-cell signaling[4], and thus the way cells are organized in a physiological environment. To investigate this aspect, we considered a volumetric imaging approach, namely light-sheet microscopy, and applied it to the investigation of a 3D cell culture of HGPS cells[5]. Notably, this is an intriguing option for multimodal analysis because it is fully compatible with 3D ptychography measurements[6].

The final goal behind these research activities was developing a multimodal optical microscope for in depth cellular biology investigations. This is an ambitious target requiring a high level of specific competence, and we pursued it in collaboration with other members of the Nanoscopy group of the Istituto Italiano di Tecnologia. Each member of the team was in charge of a specific task; mine included ptychography, fluorescence confocal microscopy, and the sample preparation for all the techniques considered in the project.

The multimodal microscope aims at answering many questions about progeria syndrome. Can we detect significant changes in terms of RI between a normal cell and an HGPS cell? Is only a morphological change connected to a variation of the optical properties of the cells, and can this information be used for biomedical applications? Yet, is the morphological change in the nucleus the cause of an abnormal organization of chromatin and thus the coding and non-coding regions of DNA? Before answering these questions, it was necessary to determine the information that each mode of the microscope can provide when used to study HGPS. Results of this preliminary study are presented in this chapter.

4.2 The Hutchinson-Gilford progeria syndrome

4.2.1 Introduction to HGPS

The word "*progeria*" comes from the Greek words "*pro*" (πρό), meaning "*before*" or "*premature*", and "gēras" (γῆρας), meaning "*old age*". As such, the term *progeria* well defines the biological implications of this disease. In particular, HGPS is a rare genetic disorder that causes premature aging beginning in childhood[7]. Patients affected by HGPS have a short life expectancy, barely reaching the twenties before they develop fatal cardiovascular complications. The disorder is caused by a mutation of the gene, which encodes a protein that constitutes the skeleton of the nucleus, namely the nuclear lamina. The nuclear laminar is a fibrillar network inside the nucleus of eukaryote cells, located beneath the inner face of the inner nuclear membrane (Figure 4.1A). It is composed of intermediate filaments and membrane-associated proteins. The nuclear lamina plays a key role in the nuclear compartment; it provides mechanical support to the membrane and regulates DNA replication or cell division. The lamina also participates in the chromatin organization process and anchors the nuclear pore complexes embedded in the nuclear envelope[4].

The structural components of the nuclear lamina are proteins named lamins, which can be lamin-A- and C-types. The cause of progeria was discovered to be a point mutation at position 1824 of the LMNA gene[8] (Figure 4.1B). This mutation leads to the synthesis of a truncated lamin-A protein. Without lamin A, the nuclear lamina is unable to provide the nuclear membrane with adequate structural support, causing it to assume an abnormal shape. Weakening of the nuclear lamina limits the cell's ability to divide, causes irregular DNA repair, and increases genomic instability. Therefore we expect, in agreement with the literature[9], to observe differences in the morphology and refractive index of HGPS cells with respect to healthy cells.

4.2.2 Cell culture model

To test each microscopy modality, we used Human embryonic kidney (HEK) 293 cells as a model sample of HGPS. Hereafter we will refer to the healthy model cell as HEK-293 and to the
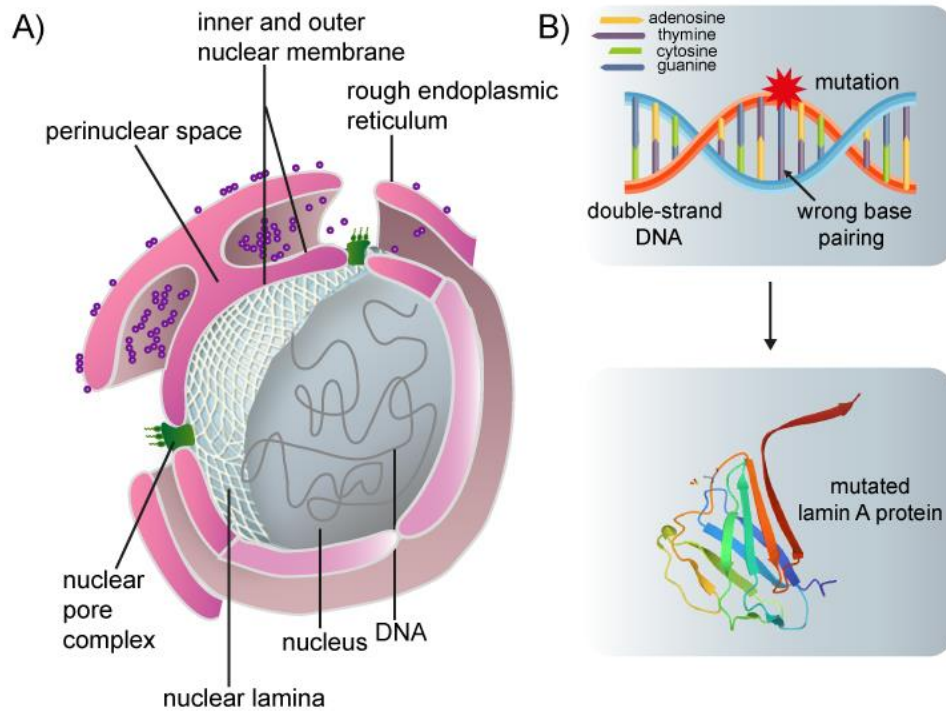
Figure 4.1. A) Nuclear lamina position and its interplay with other structures of the cell. The nuclear lamina is a stiff meshwork consisting of A-type lamins and B-type localized between the inner nuclear membrane and chromatin. Nuclear lamins interact with a wide range of nuclear proteins. B) In patients affected by HGPS, the mutation is caused by a defect in the pairing of the nitrogenous bases of the DNA, namely, a cytosine is replaced by a thymine[10]. This mutation creates an abnormal precursor of lamin protein called progerin. Being attached to the inner nuclear membrane, the latter does not become part of the lamina, resulting in an abnormal nuclear morphology and alterations of chromatin organization.

progeria model cells as HEK-progeria. As detailed next, the sample preparation followed slightly different protocols depending on the selected technique. HEK 293 cells were grown in Dulbecco's Modified Eagles Medium (DMEM High-Glucose, Gibco) + 1% l-Glutamine, supplemented with 10% fetal bovine serum (Sigma-Aldrich), 1% non-essential amino acids, and 1% pen/strep, with 5% CO_2, 90% relative humidity at 37 °C. To obtain the progeria phenotype (HEK-progeria), the HEK 293 cells were stably transfected with the plasmid simultaneously encoding the mutant protein Δ50 lamin-A and the enhanced green fluorescent protein (eGFP)

(Addgene plasmid #17653). HEK-293 and HEK-progeria were plated at 50% confluent onto an 18-mm-thick cover-glass, previously treated with a solution of poly-l-lysine (0.01%, Sigma-Aldrich) for 10 minutes to promote cellular adhesion, and grown overnight. After fixation with 4% paraformaldehyde for 10 minutes at room temperature, cells were rinsed twice for 5 minutes with fresh PBS.

For fluorescence confocal microscopy, cell nuclei of both HEK-progeria and HEK-293 were stained with a solution of 4 μM of Hoechst 33342 (10 mg/mL, ThermoFisher) for 20 minutes and rinsed twice with phosphate-buffered saline (PBS). Since the HEK-293 were not transfected, their lamin-A protein was stained using a conventional immunostaining protocol. Precisely, after fixation, cells were incubated in Blocking Buffer (3% Bovine Serum Albumin, 0,2% Triton 100X in PBS) for 1 hour at room temperature (RT). The incubation with primary antibody (anti-lamin-A antibody, ab26300 from AbCam, dilution 1:1000, in 3% BSA in PBS) was performed overnight at 4 °C. After three washes in PBS, the sample was incubated with a secondary antibody (AlexaFluor 488, dilution 1:200, in 3% BSA in PBS) for 1 hour at RT. Finally, cells were washed three times with PBS.

For polarization-resolved microscopy, the samples were mounted on glass slides using 10 μl of Prolong Antifade mounting medium. For ptychography measurements, we did not stain the nuclei with Hoechst 33342 to preserve the purity (refractive index) of the sample. Moreover, we didn't use any mounting medium, but only a drop of PBS released on top of the glass substrate.

For light-sheet microscopy, we prepared spheroids samples using HEK-progeria. Starting from a dish of confluent cells, we diluted them to form a suspension of 10000 cells/mL that we seeded into 96-well microplates (Corning Spheroid Microplate). After three days of growth, we fixed the spheroids with 4% paraformaldehyde for 30 minutes at RT, and we cleared the cells with Rapiclear 1.47 for 10 minutes (Sun Jin Lab co.). This clearing protocol for light-sheet microscopy is widely used since it reduces the natural opaqueness of thick samples, making accessible the investigation of large volumes at micrometer resolutions[11]. Once prepared, we embedded the spheroids into a 2% agarose gel cylinder for imaging.

4.3 Multimodal analysis of HGPS cells

Before testing the cell models with the selected microscopy modalities, we performed a preliminary experiment to prove that information coming from each mode can be fairly compared, meaning that their spatially resolved information can be co-localized. To this end, we tested a simple cell model, namely onion cells, with both ptychography and fluorescence microscopy. For the fluorescence imaging, we did not perform any labeling procedures and instead exploited the auto-fluorescence that onion cells exhibit if illuminated with a laser of wavelength 561 nm. Results of this multimodal study are shown in Figure 4.2. A good level of co-localization is evident with specific cell features such as membranes, nuclei, and organelles, clearly visible in all instances, especially in the phase map and in the fluorescence image. Once we proved that co-localization of the information is possible, we focused our attention on the biological model of the progeria syndrome.
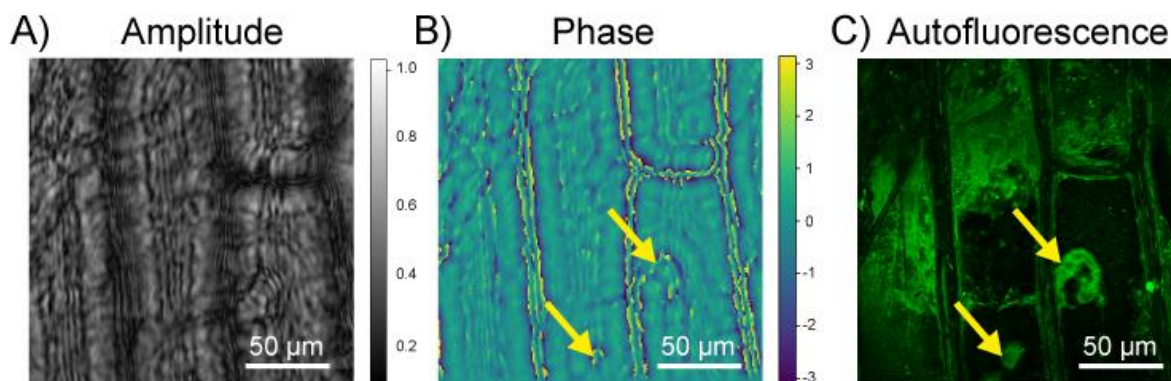

Figure 4.2. Label-free and autofluorescence co-localization in onion cells. A) and B) show respectively the reconstructed amplitude and phase. C) Onion cells autofluorescence. Yellow arrows in B) and C) highlight the presence of specific structures of the cells that exhibit a strong and localized auto-fluorescence signal and a different response to the phase with respect to the cytoplasm. The auto-fluorescence signal of onion cells, and more in general of many vegetable cells, is due to the presence of chloroplasts (emission 675-680 nm) and anthocyanins (600-630 nm) [12].

4.3.1 Confocal Imaging

Fluorescence images of both healthy and progeria cells were collected with a commercial confocal microscope (Leica TCS SP5). As shown in Figure 4.3A and C, we can appreciate valuable differences in the morphology of HEK-progeria and HEK-293. Indeed, we can see the distorted nuclear lamina in HEK-progeria, while a quite regular and rounded shape can be appreciated for HEK-293. Moreover, the analysis of a Z-stack of both HEK-progeria and HEK-293 (Figure 4.3B, D) helped us to calculate the diameter of the nucleus, which is ~10 μm, and also the thickness of approximately 4 μm.
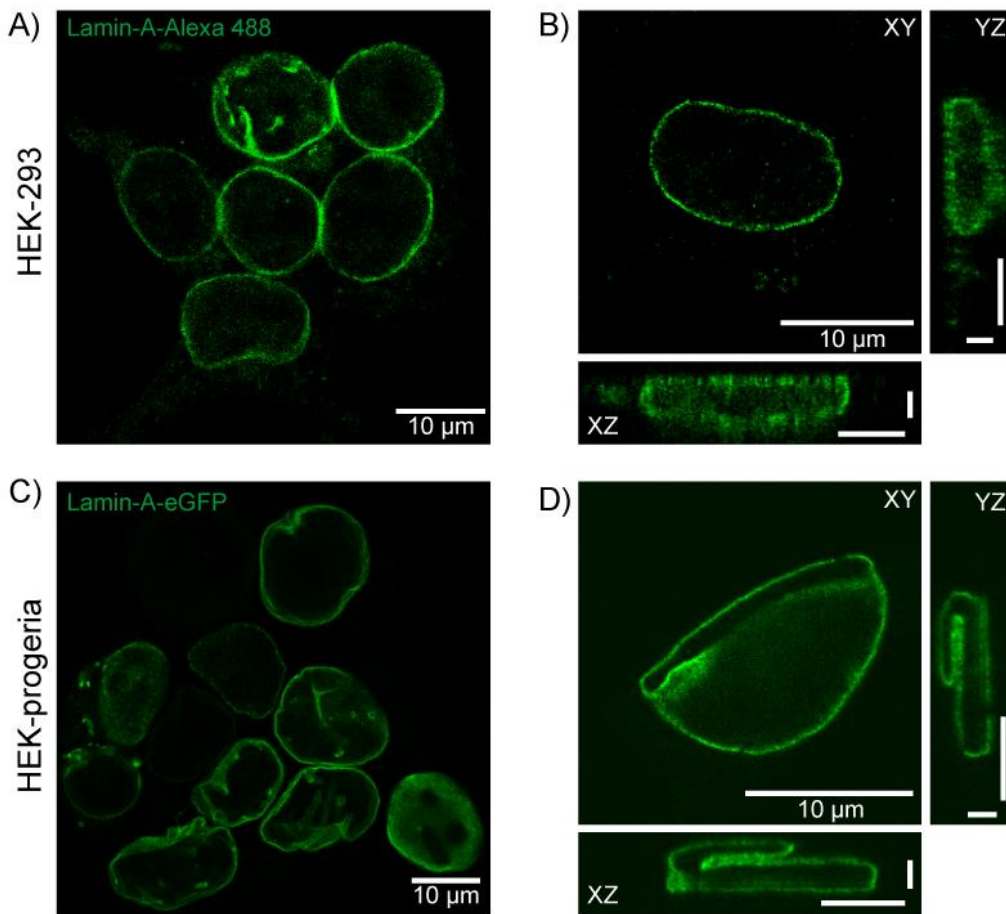

Figure 4.3. Progeria studies with fluorescence confocal microscopy A) Confocal imaging of HEK-293 and B) the orthogonal view of a single cell (YZ and XZ scale bars: 2 and 5 μm). C) Confocal imaging of HEK-progeria and D) the orthogonal view of a single cell (YZ and XZ scale bars: 2 and 5 μm, respectively).

This provides helpful information for the quantitative measurements of the refractive index for ptychography. This result validates our biological model and confirms that our strategies based on the transfection of HEK cells were successful. On the other hand, the first microscopy mode we tested suffices as a screening test for discriminating between healthy and unhealthy cells. Notably, in this proof of concept study, we did not explore fluorescence microscopy fully because this thesis focuses on the label-free analysis of biological samples. However, other features of fluorescence microscopy, such as life-time analysis or multicolor imaging, can expand the information that this mode may provide. This can be imaged as a possible future research path for researchers working in the field.

4.3.2 Light-sheet Fluorescence Microscopy

With the aim of studying the 3D organization of progeria cells and assessing whenever it is a marker of the syndrome, we also performed light-sheet fluorescence microscopy on HEK-progeria spheroids. A schematic description of the imaging procedure is shown in Figure 4.4A. Readers interested in the details of the microscope architecture can read our recent paper[5]. Briefly, the system uses a parallelized illumination (e.g., multiple light sheets) for sectioning the spheroid while the fluorescence is collected by a microscope objective orthogonal to the illumination planes. A reconstruction algorithm based on matrix formalism allows the reconstruction of a 3D image. Figure 4.4B shows a representative volumetric image of a HEK-progeria spheroid. In particular, its shell has a radius of approximately 150 μm. Moreover, the nucleus size ~ 10 μm is consistent with the measurements obtained using confocal microscopy. The variability in the transfection efficiency resulted in a non-uniform signal of the lamin for the cells composing the spheroid; however, the 3D organization of the sample remains clearly visible. This analysis indicates that HEK-progeria cells can successfully form a 3D culture despite their altered morphology, suggesting that the genetic anomaly does not affect cellular signaling. Our observations, however, are not conclusive as the COVID-19 pandemic situation limited our access to the labs, impeding our ability to perform the remaining and necessary experiments such as labeling specific structures involved in the intercellular signaling and imaging a spheroid of HEK-293 cells used as a benchmark. This possibility surely represents an intriguing research path for future students of our group.
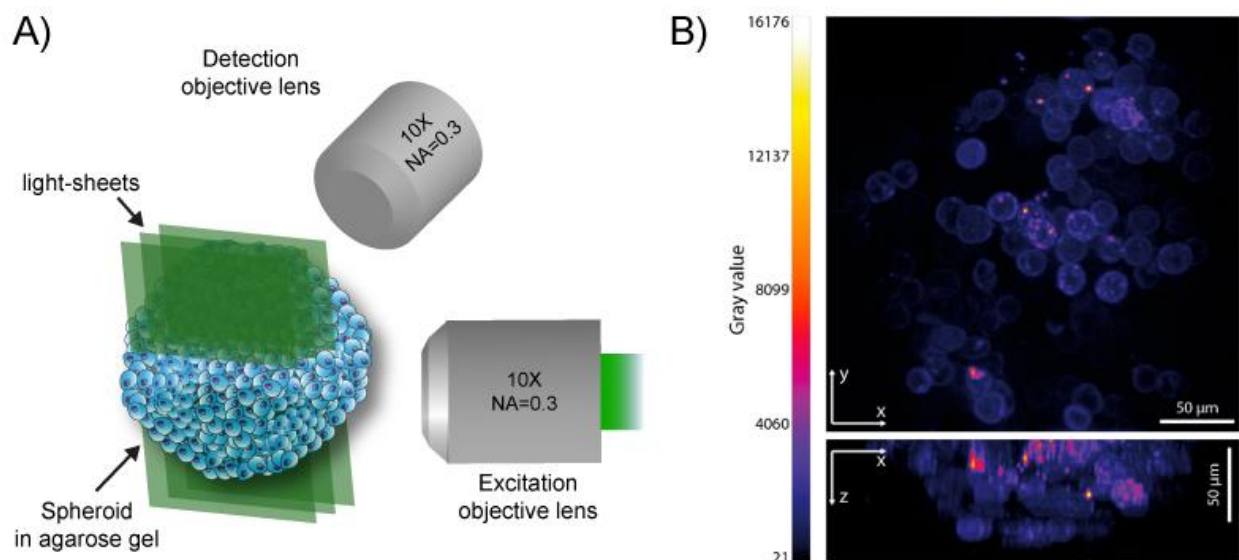
Figure 4.4. A) Schematic representation of the light-sheet microscopy principle. An excitation objective lens projects onto the sample multiple light-sheets. A second objective lens, orthogonal to the illumination planes, collects the fluorescent signal. B) Orthogonal view of the HEK-progeria spheroid[5].

4.3.3 Ptychographic Imaging

Once we validated the protocols for preparing our model cells, we moved to study the progeria syndrome with label-free approaches. The first label-free mode we exploited was ptychography. Figure 4.5 shows a superimposition of the reconstructed amplitude and phase images of a cluster of a few HEK-293 and HEK-progeria cells. We decided to overlap the information coming from the amplitude and phase to better localize the cells in the images. Indeed, differently from the experiments with the onion cells, we failed in co-localizing cells imaged with ptychography and fluorescence microscopy. We believe that this problem is due to the spatial resolution (~ 1 µm) of our microscope, which is too low with respect to the cell size. Because of this level of uncertainty, the ptychographic approach led to semi-quantitative results only. Indeed, both experiments resulted in a flat phase with the exception of some crests surrounding the cells, with those of the HEK-293 cells being more pronounced than those of the HEK-progeria cells. According to the amplitude images, the regions of the flat phase could be

associated with the surrounding medium and the crests to the cell/nuclear membrane. To better highlight this feature, we subtracted the background phase and observed the phase contrast difference between the "cell-regions" and the surrounding medium. Results of this study are shown in the histograms of Figure 4.5. For both the studied models, the majority of the pixels mapped the medium and, of course, they have a phase contrast of zero, whereas the pixels corresponding to the crests have a phase contrast between -0.5 and 0.5 radians. However, a clear difference exists between the two cell models; the number of pixels that identify the crests is significantly larger (~ a factor of 2) for the HEK-293 sample with respect to the HEK-progeria, even though the size and number of cells in the field of view are comparable.
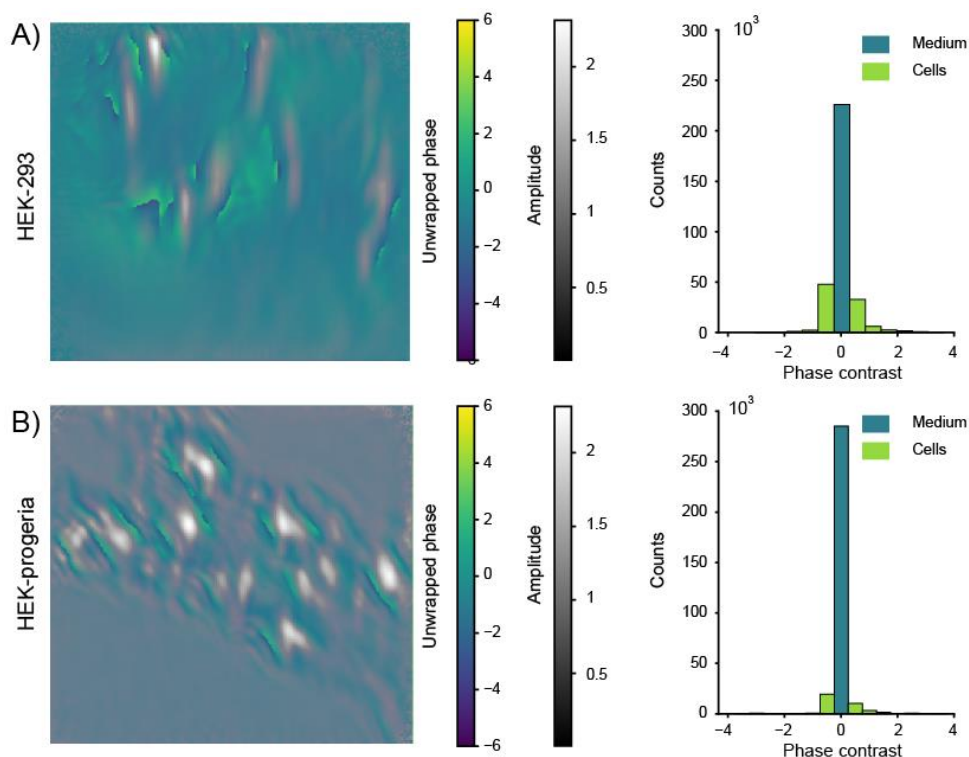

Figure 4.5. Progeria studies with ptychography. Superimposed amplitude (gray map) and unwrapped phase (color map) of (A) HEK-293 cells and (B) HEK-progeria cells. The bright spots identify the cell positions. The histograms compute the distribution of the measured phase contrast restively to the background, namely, the cell phase with respect to the mounting medium. The imaging was performed by collecting 5 images with 10 ms of exposure time for every 1024 positions used for the scan. The virtual detector plane was 230 μm above the sample plane and the illumination plane 5 μm below the sample plane.

This feature might be the sign of a lower refractive index and, thus, representative of the level of chromatin compaction in the progeria cells. Unfortunately, the limits of our current ptychographic setup, and the time limitations of the COVID-19 pandemic, didn't allow us to provide a final and definitive answer to the biological question we selected. As detailed next, we decided to exploit the transmitted light to study the cell models with another source of specimen contrast, namely, the polarization of light.

4.3.4 Polarization-resolved microscopy

The polarization of light, as introduced in chapter 1, is another label-free method to provide contrast to a specimen on the basis of its optical anisotropy. Polarized light microscopy applies well to chromatin studies because polarization is sensitive to the molecular organization and cellular/nuclear shape. Being an aggregate of proteins and chiral molecules, chromatin exhibits a strong interaction with circularly polarized light[13], and this light-matter interaction can be used to diagnose genetic pathology, including progeria syndrome. To this end, we performed polarimetric measurements of both HEK-293, used as a reference sample, and HEK-progeria and analyzed the collected data by means of phasor analysis[3]. In this study, fluorescence (i.e., two-photon excitation) microscopy and polarized light microscopy were implanted on the same microscope. A photoelastic modulator was used to modulate at 50 kHz the intensity of incident light. A lock-in amplifier was used to retrieve the modulated component of light after interacting with the sample. The fluorescence signal, namely the nuclei (Hoechst 33342) stain, was used to confirm the presence of the target DNA and select a region of interest (ROI) to retrieve the modulation and phase of the recorded signals. The stain of the lamin-A, on the other hand, is used as a benchmark to confirm the presence of the genetic mutation. Figure 4.6A shows the fluorescence images and the retrieved both modulation and phase maps for HEK-progeria and HEK-293, respectively. The fluorescence images allowed the determination of the ROI with the target DNA. Interestingly, the modulation image of the HEK-progeria exhibited a clear contrast reduction with respect to the healthy reference. Simply put, the deformed shape of the progeria cell leads to stronger scattering. This agrees well with the phase images where the phase contrast of the HEK-progeria almost vanishes, whereas a residual contrast still exists in the healthy cell. We believe that such extremely low modulation and phase contrast can be ascribed to the lower
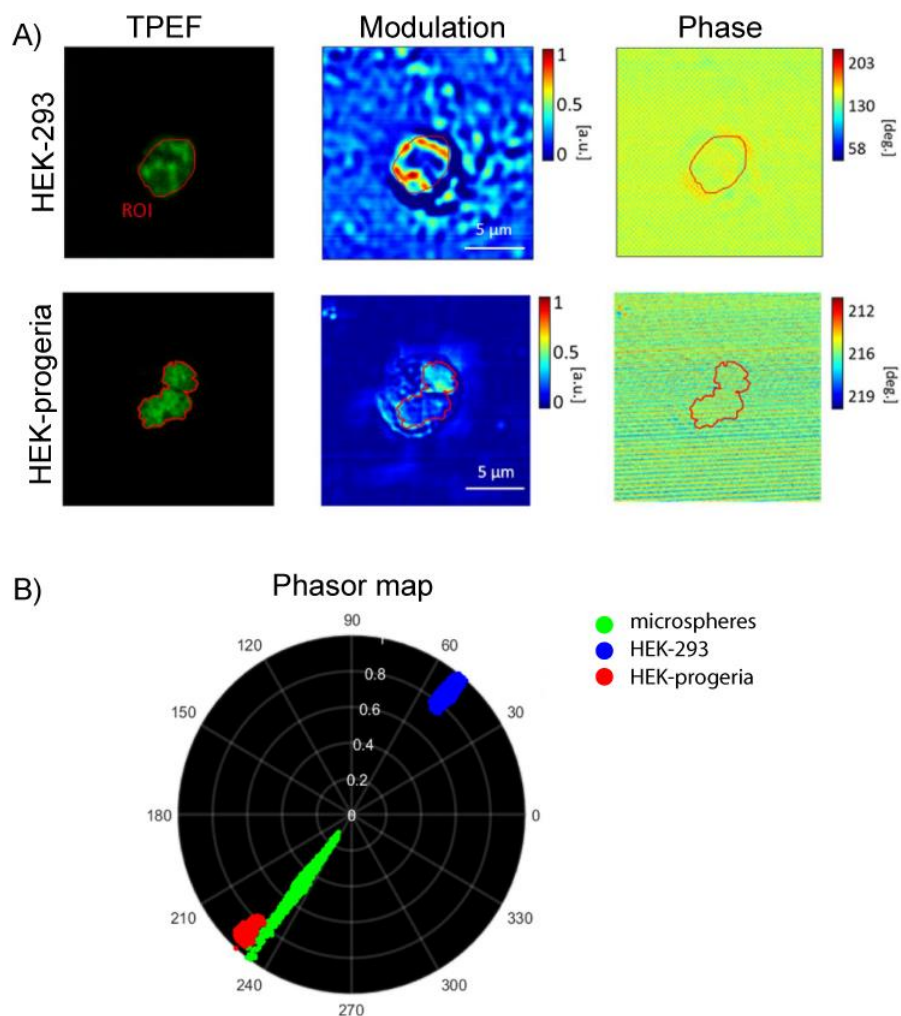
Figure 4.6. A) Two-Photon Excitation Fluorescent (TPEF) images of isolated HEK-293 nucleus and HEK-progeria compared to corresponding polarimetric modulation and phase images. B) Image phasor map of microspheres as a reference, control HEK-293 cell data compared to HEK-progeria cell discriminated by green, blue and red, respectively.

level of chromatin compaction inside the nuclear membrane of progeria cells. This is the main point that allowed us to discriminate healthy HEK cells from the progeria ones on the phasor map (Figure 4.6B).

4.4 Conclusions

In this chapter, we reported on the application of a multimodal optical microscopy approach to the study of Hutchinson-Gilford progeria syndrome. To this end, we successfully developed models of healthy cells, used as a reference, and cells affected by the syndrome. As a proof of concept, we studied these models with three modes; fluorescence, ptychography, and polarization-resolved microscopy. The fluorescence microscopy validated the biochemistry behind the preparation of the models and provided vital information about cell size, localization, and morphology. The ptychography measurements led to semi-quantitative results suggesting that the phase and/or refractive index of the cell/nucleus membrane might be a label-free marker of the syndrome. This hypothesis was finally confirmed by performing polarization-resolved microscopy on the same cell models. Precisely, we found that both the phase and the modulation of circularly polarized light are altered accordingly to the level of compaction of chromatin in HGPS cells. As such, healthy and unhealthy cells can be immediately discriminated without the need for laborious and expensive labeling procedures.

Our results, even though preliminary, indicate that multimodal microscopy is the tool of choice to study complex biological problems such as genetic disorders. We are also aware that there are chances for improvements. First of all, we need to integrate the multi microscopy modalities on the same microscope in other to improve co-localization of the target cells and, thus, the reliability of our measurements. With specific reference to ptychography, we need to improve the spatial resolution of our system. This is an essential step since it exploits the microscope as a refractive index imaging system, offering the possibility of studying relevant biological questions in a label-free modality. In this regard, the synergistic combination of ptychography with polarized light microscopy, as indicated in this study, is an intriguing path to achieve a totally label-free multimodal microscope. The possibilities are not limited to light polarization but can expand to other label-free approaches or specimen contrasts, such as non-linear microscopy or atomic force microscopy.

As the integration capabilities of optical microscopes increase and we know more about light-biological matter interactions, novel and intriguing opportunities for studying biological problems will continue to emerge.

Bibliography

1.   Woodcock, C. L. & Horowitz, R. A. Chromatin organization re-viewed. *Trends Cell Biol.* **5**, 272–277 (1995).

2.   Hübner, M. R., Eckersley-Maslin, M. A. & Spector, D. L. Chromatin organization and transcriptional regulation. *Curr. Opin. Genet. Dev.* **23**, 89–95 (2013).

3.   Mohebi, A. *et al.* Phasor map analysis to investigate Hutchinson–Gilford progeria cell under polarization-resolved optical scanning microscopy. *Sci. Rep.* **12**, 1–10 (2022).

4.   Piekarowicz, K. *et al.* The effect of the lamin A and its mutants on nuclear structure, cell proliferation, protein stability, and mobility in embryonic cells. *Chromosoma* **126**, 501–517 (2017).

5.   Zunino, A. *et al.* Multiplane Encoded Light-Sheet Microscopy for Enhanced 3D Imaging. *ACS Photonics* **8**, 3385–3393 (2021).

6.   Li, P. & Maiden, A. Multi-slice ptychographic tomography. *Sci. Rep.* 1–10 (2018). doi:10.1038/s41598-018-20530-x

7.   Pollex, R. L. & Hegele, R. A. Hutchinson-Gilford progeria syndrome. *Clin. Genet.* **66**, 375–381 (2004).

8.   Hutchinson, J. Case of congenital absence of hair, with atrophic condition of the skin and its appendages, in a boy whose mother had been almost wholly bald from alopecia areata from the age of six. *Lancet* 923 (1886).

9.   Steelman, Z. A., Eldridge, W. J., Weintraub, J. B. & Wax, A. Is the nuclear refractive index lower than cytoplasm? Validation of phase measurements and implications for light scattering technologies. *J. Biophotonics* **10**, 1714–1722 (2017).

10.   Scaffidi, P. & Misteli, T. Reversal of the cellular phenotype in the premature aging disease Hutchinson-Gilford progeria syndrome. *Nat. Med.* **11**, 440–445 (2005).

11.   Rocha, M. D. *et al.* Tissue Clearing and Light-sheet Microscopy: Imaging the Unsectioned Adult Zebra Finch Brain at Cellular Resolution. *Front. Neuroanat.* **13**, (2019).

12.   Krause, G. H. & Weis, E. Chlorophyll Fluorescence and Photosynthesis: The Basics. *Annu. Rev. Plant Physiol. Plant Mol. Biol.* **42**, 313–349 (1991).

13.   Ippolito, S. Polarized high-resolution imaging. *Nat. Photonics* **2**, 273–274 (2008).

Conclusions and perspectives

Conclusions

This thesis presents an in depth study on the possibility of using optical ptychography as a quantitative label-free tool for cellular biology studies. To this end, we constructed and characterized a compact optical ptychographic microscope. We designed the system easy to attach to a large variety of commercial microscopes, opening the possibility for multimodal microscopy studies. The ePIE image reconstruction algorithm used provided clear amplitude and phase images of various samples, including organic and inorganic specimens, with successful images formed using a minimum of 20 iterations. In this case, the experimental characterization of the ptychographic microscope estimated a worst-case spatial resolution of ~ 2 µm with an image contrast close to the ideal unity value.

The ptychographic system exhibited remarkable sensing performance with excellent phase contrast sensitivity (5.34×10^6 rad/m·RIU) and an extremely low detection limit (8.8×10^{-7} m·RIU). Notably, once turned into thickness sensitivity (i.e., for a sample with homogenous refractive index), this study indicated that the system could operate as an optical profilometer with an axial resolution as low as 300 nm. As a refractive index imaging system (i.e., for a sample with known thickness), the microscope showed a modest detection limit of ~0.04 RIU for relatively large samples (>10 µm), whilst still being compatible with live-cell imaging and thus cellular biology studies.

The proof of concept work on the diagnostic capabilities of genetic disorders was given by studying the Hutchinson-Gilford progeria syndrome. For this study, ptychography was one of the microscopy modalities we explored alongside confocal, light-sheet, and light-polarized microscopy. The fluorescence modes (confocal and light-sheet) proved the success of the cell models we used and offered useful insights about cell localization, size, and organization. The ptychographic mode provided noticeable differences in the phase of healthy and progeria-suffering cells, though the results remained semi-quantitative because of the poor cell localization we obtained, arguably due to the limited spatial resolution of the system. However,

polarization resolved microscopy confirmed that the phase of a light wave interacting with cells could be used as an indicator of the syndrome.

In conclusion, this work demonstrated that ptychography is a versatile technique that can be easily implemented on standard microscopes providing consistent measurements of the phase. Despite its low spatial resolution, our microscope proved its feasibility as a quantitative phase imaging system with excellent sensitivity and good detection limit, both suitable for the label-free analysis of biological samples. Although we are aware that there is room for further improvements (see next section), this thesis represents a step forward in the realization of a totally label-free multimodal microscope for biological studies.

Future works

The work presented in this thesis has only partially shown the potentialities of ptychography for biology studies. For instance, the possibility to extend this approach to 3D imaging has been anticipated (section 4.1), along with its feasibility as a crucial inclusion in a multimodal microscope for the simultaneous collection of multiple types of data. All these options surely represent valuable ideas for future works. Nevertheless, it is worth mentioning the major problem of our system, namely its limited lateral resolution. Solutions to this problem include both computational and experimental approaches[1]. As we demonstrated, ptychography is easy to implement into commercial microscopes; thus, it can be coupled with other microscopy techniques, including those that provide super-resolution.

A valuable example is Structured Illumination Microscopy (SIM)[2]. SIM is a wide-field technique where a movable diffraction grating is inserted into the excitation beam path. The resulting spatially structured patterns are used to illuminate the sample generating multiple interference patterns. By mathematically deconvolving the interference signal, a super-resolution image is obtained. We believe that SIM is a good fit for ptychography since: 1) it is already known that a structured probe increases the lateral resolution of ptychography[3-4-5]; 2) SIM applies to either fluorescence or label-free signals[6]; 3) to reconstruct a super resolved image, SIM needs at least 9 images, this means that it collects multiple data from a single position, an aspect that ptychography already does[7]; 4) if used with labeled samples, SIM allows combing

ptychography and fluorescence on the same microscope for multimodal studies and efficient co-localization of specific features of the sample[8-9]. Although the implementation of this possibility still requires a significant effort, we believe that the path is set, and the results of this thesis surely represent a solid base for such prospective.

As we know more about structured light, its interaction with biological samples and the integration capabilities of optical microscopy evolve, interesting possibilities will continue to emerge, providing fruitful opportunities for the application of optical studies to cellular biology.

Bibliography

1. Maiden, A. M., Humphry, M. J., Zhang, F. & Rodenburg, J. M. Superresolution imaging via ptychography. *J. Opt. Soc. Am. A* **28**, 604 (2011).

2. Aminski, C. L. F. K. Frontiers in structured illumination microscopy. **3**, (2016).

3. Mudry, E. *et al.* Structured illumination microscopy using unknown speckle patterns. *Nat. Photonics* **6**, 312–315 (2012).

4. Guo, K. *et al.* 13-Fold Resolution Gain Through Turbid Layer Via Translated Unknown Speckle Illumination. *Biomed. Opt. Express* **9**, 260 (2018).

5. Dong, S., Nanda, P., Shiradkar, R., Guo, K. & Zheng, G. High-resolution fluorescence imaging via pattern-illuminated Fourier ptychography. *Opt. Express* **22**, 20856 (2014).

6. Masters, B. R. Structured Illumination Microscopy. *Springer Ser. Opt. Sci.* **227**, 233–260 (2020).

7. Maiden, A. M., Rodenburg, J. M. & Humphry, M. J. Optical ptychography : a practical implementation with useful resolution. **35**, 2585–2587 (2010).

8. Shi, X., Burdet, N., Batey, D. & Robinson, I. Multi-Modal Ptychography: Recent Developments and Applications. *Appl. Sci.* **8**, (2018).

9. Zheng, G. Fourier ptychography for multimodal imaging. in *Frontiers in Optics 2015* FTh3G.2 (Optica Publishing Group, 2015). doi:10.1364/FIO.2015.FTh3G.2

List of Publications

Papers

Trianni, A., Anthony, N., Diaspro, A., Surdo, S. "Quantitative phase and refractive index analysis using optical Ptychography". **(2022)** (*In preparation*)

Mohebi, A., Le Gratiet, A., **Trianni, A**., Callegari, F., Bianchini, P., & Diaspro, A. "Phasor map analysis to investigate Hutchinson–Gilford progeria cell under polarization-resolved optical scanning microscopy". Scientific Reports, 12(1), 1-10. **(2022)**

Zunino, A., Garzella, F., **Trianni, A.**, Saggau, P., Bianchini, P., Diaspro, A., & Duocastella, M. "Multiplane Encoded Light-Sheet Microscopy for Enhanced 3D Imaging". ACS Photonics, 8(11), 3385-3393. **(2021)**

Conference Proceedings

Trianni, A., Anthony, N., Cainero, I., & Diaspro, A. "Sim-Ptychography Imaging of Hutchinson-Gilford Progeria Syndrome (HGPS) Cells". Biophysical Journal, 120(3), 180a-181a. **(2021)**

Trianni, A., Anthony, N., Cainero, I., & Diaspro, A. "SIM-Enhanced Ptychography Imaging of Hela Cells". Biophysical Journal, 118(3), 312a. **(2020)**

List of presentations

Invited Lecturer

6th Nic@IIT Practical Workshop on Advanced Microscopy. Istituto Italiano di Tecnologia, Genova. November 30th – December 3rd. **(2021)**

Oral presentations

Trianni, A., Anthony, N., Diaspro, A. "Label Free Quantitative Phase Imaging of Hutchinson–Gilford Progeria syndrome (HGPS) cells". 13th European Biophysics Congress, Vienna, Austria. **(2021)**

Poster presentations

Trianni, A., Anthony, N., Cainero, I., Diaspro, A. "SIM-Ptychography imaging of Hutchinson–Gilford Progeria syndrome (HGPS) cells". Biophysical Society 65th Annual Meeting. **(2021)**

Trianni, A., Anthony, N., Cainero, I., Diaspro, A. "SIM-Enhanced Ptychography Imaging of HeLa Cells". Biophysical Society 64th Annual Meeting, San Diego, California. **(2020)**

Trianni, A., Anthony, N., Cainero, I., Bianchini, P., Diaspro, A. "Label Free Imaging with Super-Resolved Ptychography". International School on Nanoscale Optical Microscopy, Palazzo Loredan, Venice. **(2019)**

Acknowledgments

Dopo aver iniziato questo percorso ho subito capito che non sarebbe stato semplice, sopratutto il mettersi alla prova in un ambito completamente diverso dal mio di provenienza. Ma tra i vari intoppi, i traslochi e una pandemia è arrivata davvero la fine. Questo dottorato è stato denso di esperienze, ho imparato tanto, ho riso e ho pianto, mi son arricchita, sia scientificamente che personalmente, ma nonostante I traguardi raggiunti e non, ciò che mi ha aiutato ad arrivare alla consegna di questo document è stato avere accanto le tante persone che mi sono state vicine in questi 3 anni e che sento il bisogno di ringraziare profondamente.

Iniziando dai ringraziamenti più doverosi, ringrazio il prof. Alberto Diaspro per avermi permesso di vivere questa esperienza e avermi dato fiducia. Dr. Nicholas Anthony for being not only my supervisor but una persona